

# Characterization of the Backbone Dynamics of an Anti-Digoxin Antibody V<sub>L</sub> Domain by Inverse Detected <sup>1</sup>H–<sup>15</sup>N NMR: Comparisons With X-Ray Data for the Fab

Keith L. Constantine, Mark S. Friedrichs, Valentina Goldfarb, Philip D. Jeffrey, Steven Sheriff, and Luciano Mueller

Bristol-Myers Squibb Pharmaceutical Research Institute, Princeton, New Jersey 08543

**ABSTRACT** The dynamic behavior of the polypeptide backbone of a recombinant anti-digoxin antibody V<sub>L</sub> domain has been characterized by measurements of <sup>15</sup>N *T*<sub>1</sub> and *T*<sub>2</sub> relaxation times, <sup>1</sup>H–<sup>15</sup>N NOE values, and <sup>1</sup>H–<sup>2</sup>H exchange rates. These data were acquired with 2D inverse detected heteronuclear <sup>1</sup>H–<sup>15</sup>N NMR methods. The relaxation data are interpreted in terms of model free spectral density functions and exchange contributions to transverse relaxation rates *R*<sub>2</sub> (= 1/*T*<sub>2</sub>). All characterized residues display low-amplitude picosecond timescale librational motions. Fifteen residues undergo conformational changes on the nanosecond timescale, and 24 residues have significant *R*<sub>2</sub> exchange contributions, which reflect motions on the microsecond to millisecond timescale. For several residues, microsecond to millisecond motions of nearby aromatic rings are postulated to account for some or all of their observed *R*<sub>2</sub> exchange contributions. The measured <sup>1</sup>H–<sup>2</sup>H exchange rates are correlated with hydrogen bonding patterns and distances from the solvent accessible surface. The degree of local flexibility indicated by the NMR measurements is compared to crystallographic *B*-factors derived from X-ray analyses of the native Fab and the Fab/digoxin complex. In general, both the NMR and X-ray data indicate enhanced flexibility in the turns, hypervariable loops, and portions of β-strands A, B, and G. However, on a residue-specific level, correlations among the various NMR data, and between the NMR and X-ray data, are often absent. This is attributed to the different dynamic processes and environments that influence the various observables. The combined data indicate that certain regions of the V<sub>L</sub> domain, including the three hypervariable loops, undergo dynamic changes upon V<sub>L</sub>:V<sub>H</sub> association and/or complexation with digoxin. Overall, the 26–10 V<sub>L</sub> domain exhibits relatively low flexibility on the ps–ns timescale. The possible functional consequences of this result are considered.

© 1993 Wiley-Liss, Inc.

**Key words:** correlation time, crystallographic *B*-factor, hydrogen exchange rate, NMR relaxation, order parameter, protein motion

## INTRODUCTION

An understanding of protein function requires a detailed knowledge of both time-averaged conformations and conformational fluctuations. A number of possible roles have been suggested for protein dynamics in enzyme catalysis,<sup>1–9</sup> allosteric effects,<sup>1,2</sup> and protein–ligand binding.<sup>1,2</sup> The likelihood that some of these proposed mechanisms will prove correct is supported by recent findings. Experimental results for dihydrofolate reductase mutants<sup>10</sup> and 3-phosphoglycerate kinases<sup>11</sup> have demonstrated a correlation between enzyme dynamics and catalytic activity. The potential of protein internal motions to contribute to catalysis has been suggested by computer simulations of the serine protease mechanism.<sup>12</sup> Experimental studies of binding interactions involving proteins have indicated that minimization of conformational entropy loss may play a major role in determining binding strengths. For example, results of a <sup>1</sup>H NMR study of calbindin

Abbreviations: CDR, complementarity-determining region; C<sub>H1</sub>, constant domain 1 of the antibody heavy chain; C<sub>L</sub>, constant domain of the antibody light chain; CPMG, Carr–Purcell–Meiboom–Gill pulse sequence; CSA, chemical shielding anisotropy; EDTA, ethylenediaminetetraacetate; Fab, antibody fragment composed of the V<sub>H</sub>, V<sub>L</sub>, C<sub>H1</sub>, and C<sub>L</sub> domains; Fv, antibody fragment composed of the V<sub>H</sub> and V<sub>L</sub> domains; H3, antigen-binding loop 3 of the V<sub>H</sub> domain; HSQC, heteronuclear single-quantum coherence; *k*<sub>ex</sub>, <sup>1</sup>H–<sup>2</sup>H exchange rate; NMR, nuclear magnetic resonance; NOE, nuclear Overhauser effect; pH\*, pH meter reading uncorrected for deuterium isotope effects; *R*<sub>1</sub>, longitudinal relaxation rate; *R*<sub>2</sub>, transverse relaxation rate; *T*<sub>1</sub>, longitudinal relaxation time; *T*<sub>2</sub>, transverse relaxation time; V<sub>H</sub>, variable domain of the antibody heavy chain; V<sub>L</sub>, variable domain of the antibody light chain; 1D, one-dimensional; 2D, two-dimensional; 3D, three-dimensional.

Received June 12, 1992; revision accepted July 24, 1992.

Address reprint requests to Dr. Keith L. Constantine, Bristol-Myers Squibb Pharmaceutical Research Institute, P.O. Box 4000, Princeton, NJ 08543.

D<sub>9k</sub> revealed that the observed positive cooperativity between the two Ca<sup>2+</sup> binding sites is due primarily to a rigidification of the second site upon Ca<sup>2+</sup> binding to the first, rather than to a significant change in the time-averaged conformation.<sup>13</sup> Another example is a recent <sup>31</sup>P NMR study<sup>14</sup> of wild-type and mutant *lac* repressor headpiece-operator complexes, which suggested that "specific, strong-binding operator-protein complexes retain the inherent phosphate ester conformational flexibility . . . , whereas the phosphate esters are conformationally restricted in the weak binding operator-protein complexes." This latter result, in particular, supports the postulate that specificity and affinity may be significantly influenced by dynamical factors.<sup>1,2</sup>

Immunoglobulin fragments provide ideal systems for investigating the influence of molecular motions on binding interactions and antibody-catalyzed reactions.<sup>15</sup> Changes in the time-averaged conformations of antibodies and antigens upon complexation have been observed by X-ray crystallography.<sup>16–21</sup> Conformational adjustments of the complementarity-determining region (CDR) loops induced by antigen binding range from very minor changes to large scale rearrangements. An example of the former is binding of the rigid, hydrophobic hapten digoxin by the 26-10 antibody,<sup>16</sup> while examples of the latter include antibody binding of flexible single-stranded DNA<sup>17</sup> and linear peptide antigens.<sup>18</sup> In particular, movements of up to 5.0 Å were observed for backbone atoms in the H3 loop of Fab 17/9 upon binding of a 36-residue fragment of influenza virus hemagglutinin.<sup>18</sup> Since the H3 loop was well defined in both the antigen-free and antigen-bound 17/9 Fab, the authors suggest that the binding involves an induced fit without a significant change in the H3 conformational entropy. If this is indeed the case, the antigen-bound H3 conformation would likely possess unfavorable strain. Such an interpretation must be regarded with caution, as crystal packing may inhibit motions in both the native (uncomplexed) and complexed Fabs. Clearly, information on the dynamic behavior *in solution* is needed before definitive conclusions can be drawn.

Two-dimensional NMR experiments based on heteronuclear correlation<sup>22,23</sup> provide a powerful approach for studying protein dynamics in solution. Site-specific <sup>1</sup>H–<sup>2</sup>H exchange rates can be determined by recording a series of HSQC spectra<sup>24</sup> after dissolving a protein in <sup>2</sup>H<sub>2</sub>O. Related methods for measuring <sup>15</sup>N and <sup>13</sup>C relaxation parameters (*T*<sub>1</sub>, *T*<sub>2</sub>, and heteronuclear NOE values) have recently been developed.<sup>25–27</sup> These data may be interpreted in terms of model-free spectral density functions,<sup>28–31</sup> yielding information on the amplitudes (via order parameters) and timescales (via correlation times and exchange contributions to *T*<sub>2</sub>) of internal motions. The backbone dynamics of uni-

formly <sup>15</sup>N-labeled staphylococcal nuclease,<sup>26</sup> interleukin-1β,<sup>31</sup> ubiquitin,<sup>32</sup> glucose permease IIA domain,<sup>33</sup> Ca<sup>2+</sup>-loaded calmodulin,<sup>34</sup> and Ca<sup>2+</sup>-loaded calbindin D<sub>9k</sub><sup>35</sup> have been characterized using these techniques. Preliminary results of a study of eglin c using a more elaborate <sup>15</sup>N-relaxation protocol have been reported.<sup>36</sup> The dynamic behavior of selectively <sup>13</sup>C-labeled leucine methyl groups in staphylococcal nuclease has been characterized.<sup>37</sup> A natural abundance <sup>13</sup>C relaxation study of a zinc finger domain has been described.<sup>38</sup> <sup>1</sup>H–<sup>2</sup>H exchange rates and <sup>15</sup>N *T*<sub>2</sub> values have been reported for a selectively labeled Fv fragment of a mouse antidansyl antibody.<sup>39</sup> The results of this latter study indicated that the H3 loop is highly mobile on the μs–ms timescale in the absence of hapten, and that hapten binding results in large reductions in the amplitudes of the H3 backbone motions.

In this paper we report an analysis of <sup>1</sup>H–<sup>2</sup>H exchange rates, <sup>15</sup>N *T*<sub>1</sub> and *T*<sub>2</sub> relaxation times, and <sup>1</sup>H–<sup>15</sup>N steady-state NOE values measured for most of the backbone HN groups of the V<sub>L</sub> domain of the anti-digoxin antibody 26-10. We have previously reported a nearly complete sequential assignment of the backbone <sup>1</sup>H resonances of this protein<sup>40</sup> based mainly on 3D <sup>1</sup>H–<sup>15</sup>N NMR data. These data demonstrated that the isolated 26-10 V<sub>L</sub> domain secondary structure and overall fold is very similar to the V<sub>L</sub> conformation within the Fab.<sup>16</sup> The results of size exclusion chromatography<sup>40</sup> indicated that the protein is predominantly monomeric at relatively high (~mM) concentrations. In the present study, the dynamic behavior of the V<sub>L</sub> domain backbone in solution is compared to structural and dynamic information derived from X-ray crystallographic data<sup>16</sup> for the V<sub>L</sub> as part of the native Fab and as part of the Fab/digoxin complex. The possible significance of these results for 26-10/digoxin interactions<sup>16</sup> and for the relatively high stability of the 26-10 V<sub>L</sub>:V<sub>H</sub> association<sup>41,42</sup> is briefly discussed.

## MATERIALS AND METHODS

### Sample Preparation

Expression and purification of <sup>15</sup>N-labeled 26-10 V<sub>L</sub> domain has been described elsewhere.<sup>40,41</sup> Protein samples used for the NMR experiments were equilibrated in osmotic shock buffer that contained 2.0 mM EDTA. The EDTA was removed during the subsequent purification steps. The samples were concentrated to ~3.4 mM in 0.50 ml of buffer containing 50 mM deuterated NaOAc, 0.001% NaN<sub>3</sub>, and 90%/10% (v/v) <sup>1</sup>H<sub>2</sub>O/<sup>2</sup>H<sub>2</sub>O (sample for relaxation measurements), or 100% <sup>1</sup>H<sub>2</sub>O (sample for <sup>1</sup>H–<sup>2</sup>H exchange measurements). pH values were adjusted to 5.5. The sample used for the relaxation measurements was degassed and then sealed under argon. The sample used for <sup>1</sup>H–<sup>2</sup>H exchange measurements was lyophilized to a dry powder and re-

dissolved in 100%  $^2\text{H}_2\text{O}$  (pH\* 5.5) immediately prior to NMR data collection.

### NMR Spectroscopy

Heteronuclear  $^1\text{H}$ - $^{15}\text{N}$  NMR experiments were recorded at 30°C (relaxation measurements) or 22°C ( $^1\text{H}$ - $^2\text{H}$  exchange measurements) with a Varian UNITY-600 spectrometer operating at 599.95 MHz for  $^1\text{H}$  and 60.80 MHz for  $^{15}\text{N}$ . For all measurements, spectral widths of 10,000 and 2,000 Hz were used for  $^1\text{H}$  and  $^{15}\text{N}$ , respectively. The  $^1\text{H}$  carrier frequency was placed on the  $^1\text{H}_2\text{O}$  or residual  $^1\text{H}^2\text{HO}$  resonance (4.76 ppm at 30°C), and the  $^{15}\text{N}$  carrier frequency was set to 120 ppm. Hypercomplex data acquisition<sup>43</sup> was used in the  $F_1$  ( $^{15}\text{N}$ ) dimension for all spectra.

The pulse sequence used to measure the steady-state  $^1\text{H}$ - $^{15}\text{N}$  NOE values is described in ref. 26. Two experiments must be recorded—one with and one without  $^1\text{H}$  saturation during the 3.0 s relaxation delay. For the former experiment,  $^1\text{H}$  saturation was achieved by a series of hard 120° pulses applied every 20 ms, and the  $\text{H}_2\text{O}$  resonance was suppressed by on-resonance low-power irradiation during the periods between the 120° pulses. For the spectrum recorded without the NOE,  $\text{H}_2\text{O}$  suppression was achieved by on-resonance low-power irradiation during the last 100 ms of the relaxation delay. Both spectra were recorded as 128  $t_1$  increments, with 64 scans per increment and 1,408 complex points in  $t_2$ .

$^{15}\text{N}$   $T_1$  and  $T_2$  relaxation times were determined using modified versions<sup>27</sup> of the pulse sequences detailed in ref. 26. The modification consists of a series of  $^1\text{H}$  180° pulses applied every 5–10 ms during the inversion-recovery ( $T_1$ ) or CPMG ( $T_2$ ) delays in order to remove the effects of cross-correlation between chemical shielding anisotropy (CSA) and dipolar relaxation mechanisms.<sup>27</sup> For the  $T_2$  experiments, the period between the  $^{15}\text{N}$  180° pulses was set to 0.9 ms. As with the NOE data, the  $T_1$  and  $T_2$  spectra were recorded as 128  $t_1$  increments with 1,408 complex points in  $t_2$ . Each  $t_1$  increment was recorded with 32 transients, with a 3.0 s relaxation delay between each scan. For the  $T_1$  data, inversion-recovery delays of 48, 160, 321, 481, 641, 802, and 962 ms were used. CPMG delays of 8.0, 23.9, 47.8, 71.7, 95.6, and 119.5 ms were employed for the  $T_2$  experiments. Cross-peak intensities ( $I$ ) for both the  $T_1$  and  $T_2$  data are expected to fit:

$$I(t) = I(0)\exp(-t/T_x), \quad x = 1, 2. \quad (1)$$

This functional form is consistent with 1D  $T_2$  measurements, but not with 1D  $T_1$  measurements, where  $I(\infty) = I_{z(\text{eq})}$ . In the  $T_1$  pulse sequences of refs. 26 and 27, magnetization is frequency labeled in  $t_1$  before the inversion-recovery delay. Thus, longitudinal magnetization that builds up during the inver-

sion-recovery period is analogous to that which would produce axial peaks; it is removed by the phase cycling. The result is a decay of  $t_1$ -labeled magnetization to zero at a rate given by  $R_1$  ( $=1/T_1$ ).

$^1\text{H}$ - $^2\text{H}$  exchange rates ( $k_{\text{ex}}$ ) were derived from a series of 17 HSQC spectra<sup>24</sup> recorded over a time period extending from 34 min to 22,736 min after dissolving the protein in  $^2\text{H}_2\text{O}$ . These spectra were recorded as 80  $t_1$  increments with 1,024 complex points in  $t_2$ . Experiments acquired with exchange times between 34 and 127 min, between 174 and 296 min, and between 388 and 22,736 min were recorded with 8, 16, and 32 scans per increment, respectively.

The NMR spectra were processed on a Silicon Graphics INDIGO workstation using a modified version of the FELIX program (Hare Research, Inc.). The residual water signal was removed by application of low-frequency deconvolution<sup>44</sup> in  $t_2$ . The time-domain data were multiplied by cosine-bell window functions in both  $t_1$  and  $t_2$  and were then Fourier transformed into 512 real ( $F_1$ ) by 1,024 real ( $F_2$ ) point frequency-domain data matrices, with the upfield half of the  $^1\text{H}$  acquisition dimension discarded. First-order polynomial baseline correction was applied as needed in order to produce flat baselines in all spectra.

### Analysis of NMR Data

NMR relaxation parameters and  $^1\text{H}$ - $^2\text{H}$  exchange rates were evaluated on the basis of crosspeak intensities. The relative crosspeak intensities were gauged by the peak heights, since we and others<sup>33,35,38</sup> have found the heights to be more reliable measures of the intensities than the integrated volumes for these applications.\* The use of heights also allows reasonably accurate measurements to be made for moderately overlapping crosspeaks. The best-estimate crosspeak heights were determined from a parabolic fit over the three most intense points in each crosspeak along the  $F_2$  dimension. The standard deviations of the measured heights were assumed to be equal to the measured root-mean-square baseline noise in each spectrum.<sup>38</sup> All NMR data analysis was done using a database facility which has been added to FELIX.

$^1\text{H}$ - $^{15}\text{N}$  NOE values were computed from the ratio of the crosspeak intensities observed in the spectra recorded with and without the NOE. Errors in the NOE measurements are  $\sim 0.05$  NOE units on the basis of the root-mean-square baseline noise. However, larger error bounds must be used since the NOE measurements are subject to systematic errors

\*Crosspeak heights can be used as measures of the intensities when comparing crosspeaks with the same lineshapes, as with the data considered here. In other applications, e.g., complete relaxation matrix analysis<sup>45</sup> of NOESY data, crosspeak volumes must be used since the relative intensities of signals with different intrinsic lineshapes must be evaluated.

(see below).  $^{15}\text{N}$   $T_1$  and  $T_2$  values were determined from a nonlinear least-squares fitting of the data to Eq. (1) by minimization of  $\chi^2$ , which is given by

$$\chi^2 = \sum [I(T_{xi}^e) - I(T_{xi}^c)]^2 / \sigma_i^2, \quad x = 1, 2 \quad (2)$$

where "e" and "c" denote the experimental and calculated peak intensity of data point  $i$ , respectively, and  $\sigma_i$  is the experimental uncertainty in the intensity. Errors in the fitted relaxation times were evaluated by generating Gaussian random distributions of the crosspeak intensities, assuming that the measured heights were the means of distributions with the standard deviations derived from the root-mean-square baseline noise.<sup>38,46,47</sup> This procedure affords estimates of the errors in the relaxation times based on propagation of errors in the primary intensity data. This is expected to provide more reasonable error bounds than simply evaluating the goodness-of-fit, as fits based on a single set of points may, by chance, yield  $\chi^2$  values that do not reflect the actual uncertainty. A total of 300 simulated data sets for each  $T_1$  and  $T_2$  fitting were generated; the standard deviations of the mean relaxation times were subsequently determined. The same procedures were applied in deriving  $^1\text{H}$ - $^2\text{H}$  exchange rates for those HN protons which exchange slowly enough to allow for explicit fitting of  $k_{\text{ex}}$  to an exponential decay.

Dipolar and CSA contributions to the  $^{15}\text{N}$  longitudinal and transverse relaxation rates ( $R_1$  and  $R_2$ , respectively) and the NOE in an  $^1\text{H}$ - $^{15}\text{N}$  spin system are given by<sup>48</sup>

$$R_1 = 1/T_1 = d^2[J(\omega_{\text{H}} - \omega_{\text{N}}) + 3J(\omega_{\text{N}}) + 6J(\omega_{\text{H}} + \omega_{\text{N}})] + c^2J(\omega_{\text{N}}). \quad (3)$$

$$R_2 = 1/T_2 = 0.5d^2[4J(0) + J(\omega_{\text{H}} - \omega_{\text{N}}) + 3J(\omega_{\text{N}}) + 6J(\omega_{\text{H}}) + 6J(\omega_{\text{H}} + \omega_{\text{N}})] + c^2[4J(0) + 3J(\omega_{\text{N}})]/6. \quad (4)$$

$$\text{NOE} = 1 + T_1(\gamma_{\text{H}}/\gamma_{\text{N}})d^2[6J(\omega_{\text{H}} + \omega_{\text{N}}) - J(\omega_{\text{H}} - \omega_{\text{N}})]. \quad (5)$$

In these expressions,  $\omega_{\text{H}}$  and  $\omega_{\text{N}}$  are the Larmor frequencies for  $^1\text{H}$  and  $^{15}\text{N}$  ( $3.770 \times 10^9$  and  $-3.820 \times 10^8$  rad/s, respectively, in this study),  $\gamma_{\text{H}}$  and  $\gamma_{\text{N}}$  are the  $^1\text{H}$  and  $^{15}\text{N}$  magnetogyric ratios, and  $c^2$  and  $d^2$  are the products of physical constants relevant to CSA and dipolar relaxation mechanisms, respectively. The dipolar constant  $d^2$  is given by  $(1/40)\gamma_{\text{H}}^2\gamma_{\text{N}}^2\hbar^2\pi^{-2}\langle r_{\text{HN}}^{-3} \rangle^2$ , where  $\hbar$  is Planck's constant and  $r_{\text{HN}}$  is the length of the NH bond (1.02 Å). The CSA constant  $c^2$  is given by  $(2/15)\omega_{\text{N}}^2(\sigma_{\parallel} - \sigma_{\perp})^2$ , where  $\sigma_{\parallel}$  and  $\sigma_{\perp}$  are the parallel and perpendicular components of the amide NH  $^{15}\text{N}$  chemical shift tensor ( $\sigma_{\parallel} - \sigma_{\perp} = -160$  ppm). The spectral density functions,  $J(\omega)$ , are Fourier transforms of autocorrelation functions describing the motion of the NH vectors. Exchange contributions to  $R_2$ , due to motions on the  $\mu\text{s}$ -ms timescale, were treated by adding a third term  $R_{2\text{ex}} (= 1/T_{2\text{ex}})$  to Eq. (4).

Three functional forms of model-free spectral density functions<sup>28-31</sup> were used to fit the relaxation data. In order of increasing complexity, these are

$$J(\omega) = S^2\tau_r/(1 + \omega^2\tau_r^2). \quad (6)$$

$$J(\omega) = S^2\tau_r/(1 + \omega^2\tau_r^2) + (1 - S^2)\tau/(1 + \omega^2\tau^2). \quad (7)$$

$$J(\omega) = S_f^2S_s^2\tau_r/(1 + \omega^2\tau_r^2) + S_f^2(1 - S_s^2)\tau_s/(1 + \omega^2\tau_s'^2). \quad (8)$$

In these expressions,  $S^2$  is the total generalized order parameter (which depends on the amplitudes of ps-ns motions),  $\tau_r$  is the overall molecular rotational correlation time,  $\tau$  is an effective correlation time resulting from internal motions characterized by a single internal correlation time  $\tau_e$  ( $1/\tau = 1/\tau_e + 1/\tau_r$ ),  $S_f^2$  and  $S_s^2$  are order parameters corresponding to fast and slow internal ps-ns motions with timescales differing by at least an order of magnitude, respectively (note:  $S^2 = S_f^2S_s^2$ ), and  $\tau_s'$  is an effective correlation time resulting from the slower internal motions characterized by a slow correlation time  $\tau_s$  ( $1/\tau_s' = 1/\tau_s + 1/\tau_r$ ). Equation (8) is based on the assumption that the correlation time for the faster internal motions is less than  $\sim 20$  ps.<sup>31</sup>

In general, Eq. (6) is expected to give an adequate fit for HN groups in rigid (on the ps-ns timescale) regions of the structure which undergo only low-amplitude, high-frequency fluctuations within a minimum on the free energy surface. Equations (7) and (8) are designed to fit cases of internal motions occurring with significant amplitude on one or two ps-ns timescale orders, respectively. Rigorous separation of global and internal motions by the model-free approach is possible only when the internal motion is much faster than the global correlation time.<sup>28,32</sup> Therefore, Eq. (8) affords only an approximate characterization of motions that are moderately faster than the overall tumbling. Details on the criteria used for deciding which spectral density function to use for each particular residue are given in the Results section. Note that Eqs. (6), (7), and (8) contain one, two, and three adjustable parameters, respectively, as  $\tau_r$  is established independently (see Results). Since we have three independent measurements, three parameters at most can be fit by the data. This precludes use of Eq. (8) in cases where  $R_{2\text{ex}}$  must be considered.

Order parameters, correlation times, and exchange contributions, along with their error estimates, were derived from the relaxation data by numerical fitting routines.<sup>49</sup> A grid search was used to obtain the initial parameter estimates. This was followed by least squares minimization of  $\chi^2$  using the Levenberg-Marquardt algorithm,<sup>49</sup> with  $\chi^2$  given by

$$\chi^2 = [(T_1^e - T_1^c)/\sigma_{T_1}]^2 + [(T_2^e - T_2^c)/\sigma_{T_2}]^2 + [(\text{NOE}^e - \text{NOE}^c)/\sigma_{\text{NOE}}]^2 \quad (9)$$

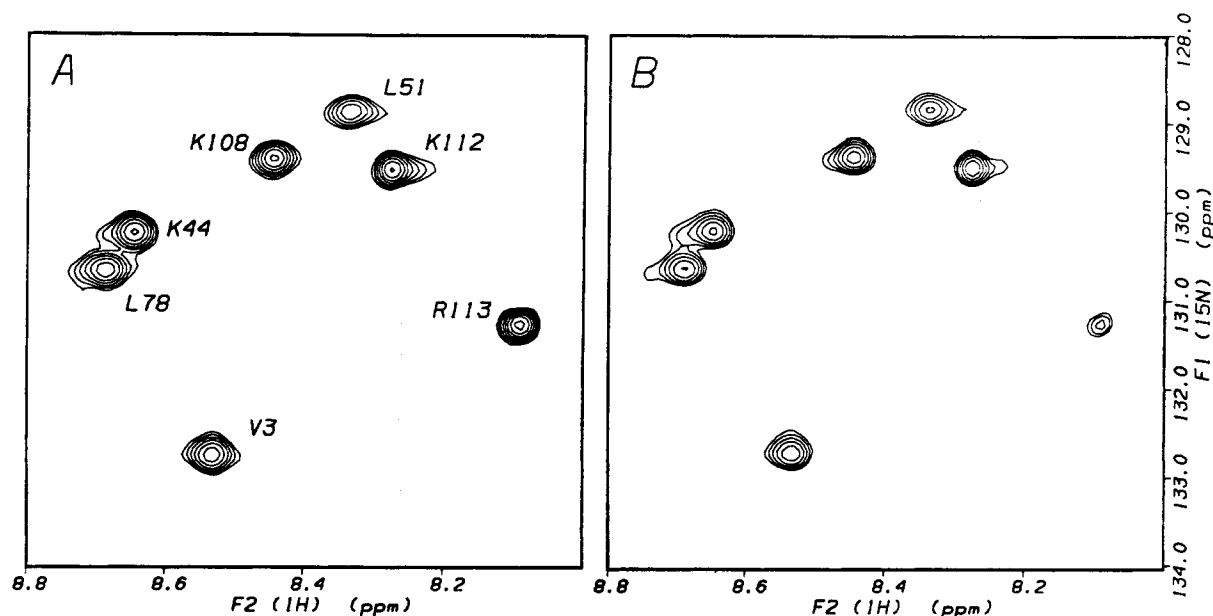


Fig. 1. The 600 MHz 2D  $^1\text{H}$ - $^{15}\text{N}$  correlation spectra from which the  $^1\text{H}$ - $^{15}\text{N}$  NOE values have been derived. (A) Small region of the spectrum recorded without  $^1\text{H}$  saturation during the relaxation delay. Crosspeaks are shown labeled. (B) Correspond-

ing region of the spectrum recorded with  $^1\text{H}$  saturation. The spectra were recorded at 30°C on a 3.4 mM  $V_L$  sample dissolved in 90%/10% (v/v)  $^1\text{H}_2\text{O}/^2\text{H}_2\text{O}$  containing 50 mM deuterated NaOAc, 0.001%  $\text{NaN}_3$ , pH 5.5.

where “e” and “c” refer to the experimental and calculated relaxation parameters, respectively, and  $\sigma_x$  is the uncertainty in relaxation parameter  $x$ . The terms involving the NOE or  $T_2$  were at times excluded from the fit (see Results). Errors in the fitted parameters were subsequently evaluated by generating 1,000 Gaussian random distributions of the primary relaxation data for each residue on the basis of the derived  $T_1$ ,  $T_2$ , and NOE values and their errors (see the Appendix).<sup>38,46,47</sup>

#### Information From Crystallographic Data

Crystallographic  $B$ -factors were derived from a restrained  $B$ -factor refinement of the X-ray models of the 26-10 Fab:digoxin complex at 2.5 Å resolution and the native Fab at 2.7 Å resolution.<sup>16</sup> Contacts were calculated with the method of Sheriff et al. (1987),<sup>50</sup> using extended atom radii.<sup>51</sup> Regions of the  $V_L$  domain surface buried by digoxin were computed with the Connolly method,<sup>52</sup> using a 1.6 Å probe sphere and extended atom radii. This is a more inclusive criterion than that used to define contacts. The solvent accessible surface was also calculated by the Connolly method with a 1.6 Å probe radius and 10 points per Å<sup>2</sup>. The X-PLOR program<sup>53</sup> was used to build standard geometry  $^1\text{H}$  coordinates on to the 26-10  $V_L$  domain derived from X-ray structure of the Fab:digoxin complex.<sup>16</sup> The distance of an amide proton to the nearest surface point was determined by a grid search. Hydrogen bond acceptor oxygen-donor hydrogen distances were also characterized. The X-ray data were used to generate Figures 8, 9,

11 and 12, which were produced using the *Insight II* program (Biosym Technologies, San Diego, CA).

## RESULTS

### $^1\text{H}$ - $^{15}\text{N}$ NOE Values and $^{15}\text{N}$ $T_1$ and $T_2$ Relaxation Times

Of the 103  $^1\text{H}$ - $^{15}\text{N}$  correlations identified in the HSQC spectrum of the 26-10  $V_L$  domain,<sup>40</sup> 89 are sufficiently resolved to allow accurate peak height measurements to be made. Figure 1A shows a small region of the  $^1\text{H}$ - $^{15}\text{N}$  correlation spectrum recorded without the NOE; the corresponding region (positive contours) of the spectrum recorded with the NOE is shown in Figure 1B. All crosspeaks in the latter experiment show reduced intensities relative to the former, with Arg-113 (the C-terminal residue) showing the most substantial difference. The average NOE value computed from the peak heights is  $0.80 \pm 0.08$ . (Crosspeak volume ratios measured for 84 residues yield a value of  $0.77 \pm 0.11$ .) Negative NOEs are not observed for any of the backbone HN groups; several side chain HN groups display such NOEs (not shown). Indeed, the only residue with a backbone  $^1\text{H}$ - $^{15}\text{N}$  NOE value  $< 0.65$  is Arg-113, which has an NOE of  $0.19 \pm 0.10$ . This indicates that nearly all 26-10  $V_L$  residues have only small amplitude motions on a timescale  $< 50$  ps.<sup>31</sup> However, NOE values must be interpreted with caution, since spin diffusion from bound  $\text{H}_2\text{O}$  and saturated  $\text{H}^\alpha$  resonances, as well as saturation transfer from the bulk solvent, may occur in the experiment recorded without the NOE due to the 100 ms  $\text{H}_2\text{O}$

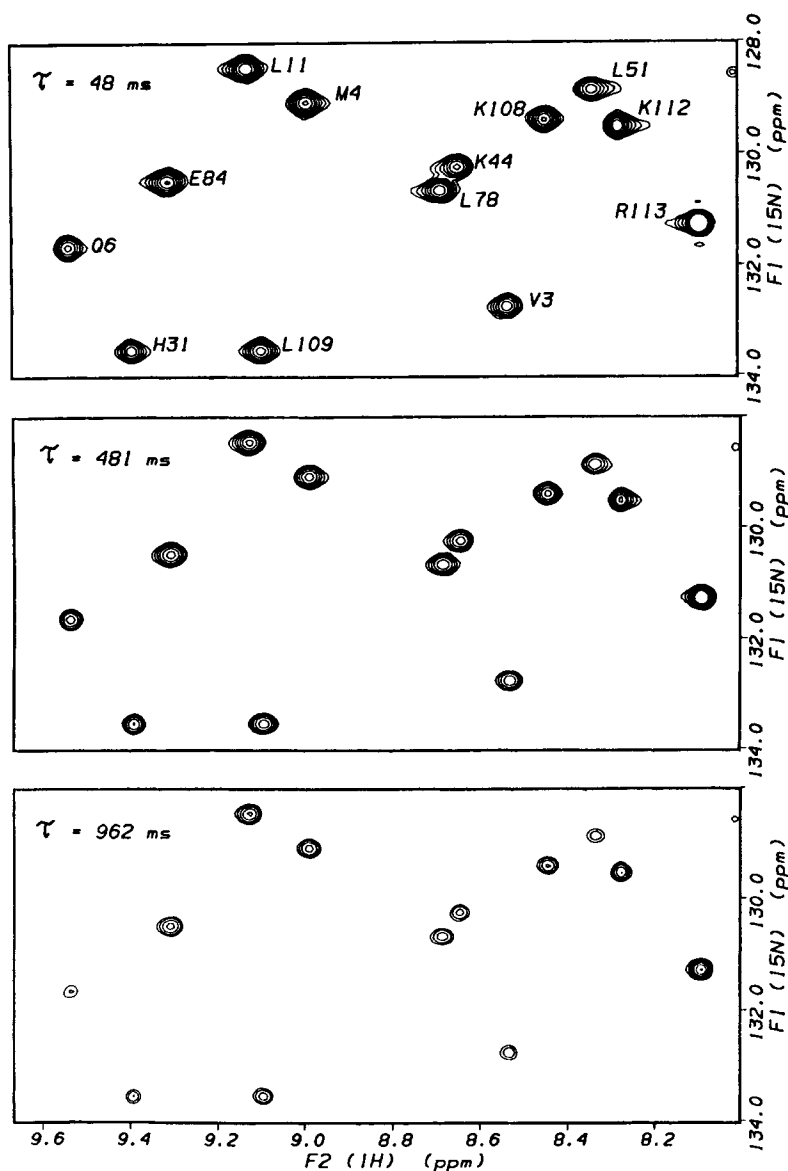


Fig. 2. Examples showing a small region of 600 MHz 2D  $^1\text{H}$ - $^{15}\text{N}$  correlation spectra from which the  $^{15}\text{N}$   $T_1$  values have been derived. The inversion-recovery delays ( $\tau$ ) are given in the upper left corners of each of the three example spectra. Crosspeaks in the displayed region are shown labeled in the upper ( $\tau = 48$  ms) spectrum. Experimental conditions are given in the caption of Figure 1.

presaturation period. These effects may cause systematic overestimation of the magnitudes of some of the measured NOE values by as much as  $\sim 0.1$  NOE units. The derived NOE values are available in the Appendix.

Examples of data used to derive  $^{15}\text{N}$   $T_1$  values are displayed in Figure 2, which shows a small spectral region for  $T_1$  data recorded with inversion-recovery delays of 48, 481, and 962 ms. Representative  $T_1$ -decay curves are illustrated in Figure 3. The corresponding region of  $T_2$  spectra recorded with CPMG delays of 8.0, 47.8, and 119.5 ms is shown in Figure 4, and example  $T_2$ -decay curves are shown in Figure

5. All of the  $T_1$  and  $T_2$  data give adequate fits to Eq. (1). The maximum error, in terms of percent of the equilibrium magnetization  $I(0)$ , between the experimental and best-fit peak intensities for the  $T_1$  data ranges from 0.6% (Leu-88) to 7.8% (Thr-96), with the majority of the maximum errors less than 2.0%. The maximum errors for the  $T_2$  data are between 0.8% (Glu-86) and 7.6% (Asn-39), with the majority less than 3.0%. The maximum and minimum  $T_1$  values are  $893 \pm 106$  ms (Thr-96) and  $592 \pm 32$  ms (Asn-39), respectively. The average  $T_1$  for 89 residues is  $700 \pm 40$  ms. The average, minimum, and maximum  $T_2$  values are  $88 \pm 15$ ,  $59 \pm 6$  (Gly-104), and  $170 \pm$

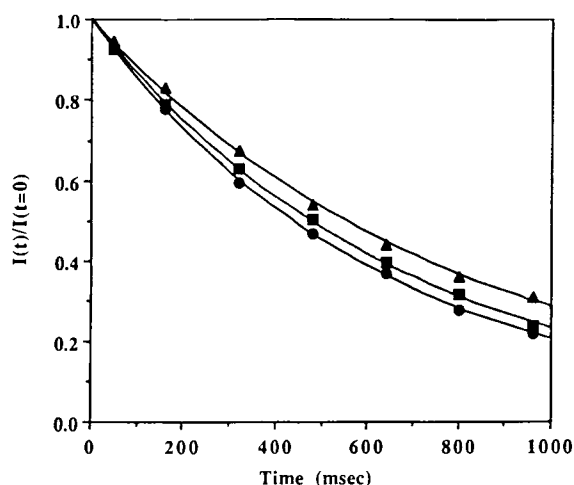


Fig. 3. Representative  $T_1$ -decay curves. Normalized experimental data points for Ser-61 ( $T_1 = 802 \pm 17$  ms), Leu-11 ( $T_1 = 687 \pm 8$  ms), and Gly-73 ( $T_1 = 634 \pm 11$  ms) are indicated by  $\blacktriangle$ ,  $\blacksquare$ , and  $\bullet$  symbols, respectively. The solid lines represent best-fit exponential decays to the experimental data.

1 ms (Arg-113), respectively. The  $T_1/T_2$  ratios range between 4.43 (Arg-113) and 14.7 (Thr-96), and the average value of the  $T_1/T_2$  ratio is  $8.17 \pm 1.48$ . The derived  $T_1$  and  $T_2$  relaxation times, and their estimated errors, are available in the Appendix.

### Fitting of Relaxation Data to Spectral Densities

The overall rotational correlation time  $\tau_r$  was determined from a preliminary analysis of the  $T_1$  and  $T_2$  data. Seventy-three residues that display  $T_1/T_2$  ratios within one standard deviation of the mean (see above) were used. For this purpose, it was assumed that the backbone motions of these residues could be described by Eq. (6). Local values of  $\tau_r$  were computed from the  $T_1/T_2$  ratios. (The dependence on  $S^2$  cancels upon taking the ratio.) This treatment yielded an average  $\tau_r$  of  $8.45 \pm 0.24$  ns. The overall  $\tau_r$  was treated as a fixed parameter for the analysis of the relaxation data in terms of Eqs. (6), (7), and (8). A strategy similar to that employed in the analysis of  $^{15}\text{N}$  relaxation data for interleukin- $1\beta$ <sup>31</sup> has been implemented. In general, the simplest form of  $J(\omega)$  that adequately fit the data was used. Also, the NOE values were used explicitly in the fitting routines only in cases where it was necessary to fit three parameters to the data. The protocol used is conveniently described by the following pseudocode:

```

If NOE > 0.8 then
  If  $T_1/T_2 > \langle T_1/T_2 \rangle$  or  $T_2 < \langle T_2 \rangle$  then
    Fit  $T_1$  and  $T_2$  with Eq. (6) and include  $R_{2\text{ex}}$ 
  Else
    Fit  $T_1$  and  $T_2$  with Eq. (6) and exclude  $R_{2\text{ex}}$ 
  End If
Else
  If  $T_1/T_2 < \langle T_1/T_2 \rangle$  then

```

```

    Fit  $T_1$  and  $T_2$  with Eq. (7) and exclude  $R_{2\text{ex}}$ 
  Else
    Fit  $T_1$ ,  $T_2$  and NOE with Eq. (7) and include  $R_{2\text{ex}}$ 
  End If
End If
Calculate  $T_1$ ,  $T_2$  and NOE values based on derived parameters.
Determine differences between calculated and experimental  $T_1$ ,  $T_2$ , and NOE values.
If  $[(\text{NOE})_{\text{exp}} - (\text{NOE})_{\text{calc}}] > 0.15$  then
  If  $T_1/T_2 > \langle T_1/T_2 \rangle$  then
    Fit  $T_1$  and NOE with Eq. (7)
    Estimate  $R_{2\text{ex}} = R_{2\text{exp}} - R_{2\text{calc}}$ 
  Else
    Fit  $T_1$ ,  $T_2$  and NOE to Eq. (8) and exclude  $R_{2\text{ex}}$ 
  End if
End If.

```

In all cases where  $R_{2\text{ex}}$  was included in the fit, the initial value was set to 0. Also, in what follows, the dynamic behavior of residues that were explicitly fit by Eq. (7) was considered to be adequately described by Eq. (6) if  $S^2 > 0.80$  and  $\tau_e \sim 10$  ps or less were found. The criteria used here to include  $R_{2\text{ex}}$  and/or internal correlation times in the fit are less restrictive than those used by Clore and co-workers in the interleukin- $1\beta$  study,<sup>31</sup> as they essentially restricted their analysis to residues falling more than one standard deviation above or below the mean  $T_1/T_2$  ratio. Monte Carlo simulations of the glucose permease IIA domain relaxation data demonstrated that less restrictive criteria are more appropriate.<sup>33</sup>

For the 89 residues whose relaxation data was treated in this manner, 59 were adequately fit by Eq. (6), 15 were fit by Eq. (7), and 15 were fit by Eq. (8). Residuals of the calculated and experimental  $T_1$  and  $T_2$  values are  $< 2\%$  for most residues. Only three residues—Gly-34, Asn-39, and Gly-71—have  $T_1$  residuals  $> 5\%$  and  $T_2$  residuals  $> 8\%$ . Significant exchange contributions to  $R_2$  were found for 24 residues. Another six residues—Ser-25, Thr-36, Ser-57, Val-63, Glu-84, and Ile-90—were found to have nonzero  $R_{2\text{ex}}$  values that were comparable to the errors in  $R_2$ ; therefore, these  $R_{2\text{ex}}$  values may be artifactual. The parameters derived for residues fit by Eq. (6), Eq. (7), or Eq. (8) are listed in Tables I, II, and III, respectively. Estimates of the errors in the parameters (see Materials and Methods) are also given. Possible additional sources of errors in model-free parameters have been discussed extensively by other groups.<sup>26,27,31–38</sup> We note that errors due to uncertainties regarding the  $c^2$  and  $d^2$  parameters of Eqs. (3)–(5) are not expected to significantly alter the results.<sup>26,32</sup>

Tables I, II, and III include the crystallographic  $B$ -factors of the  $V_L$  domain backbone nitrogens within the native and digoxin-complexed 26-10 Fab

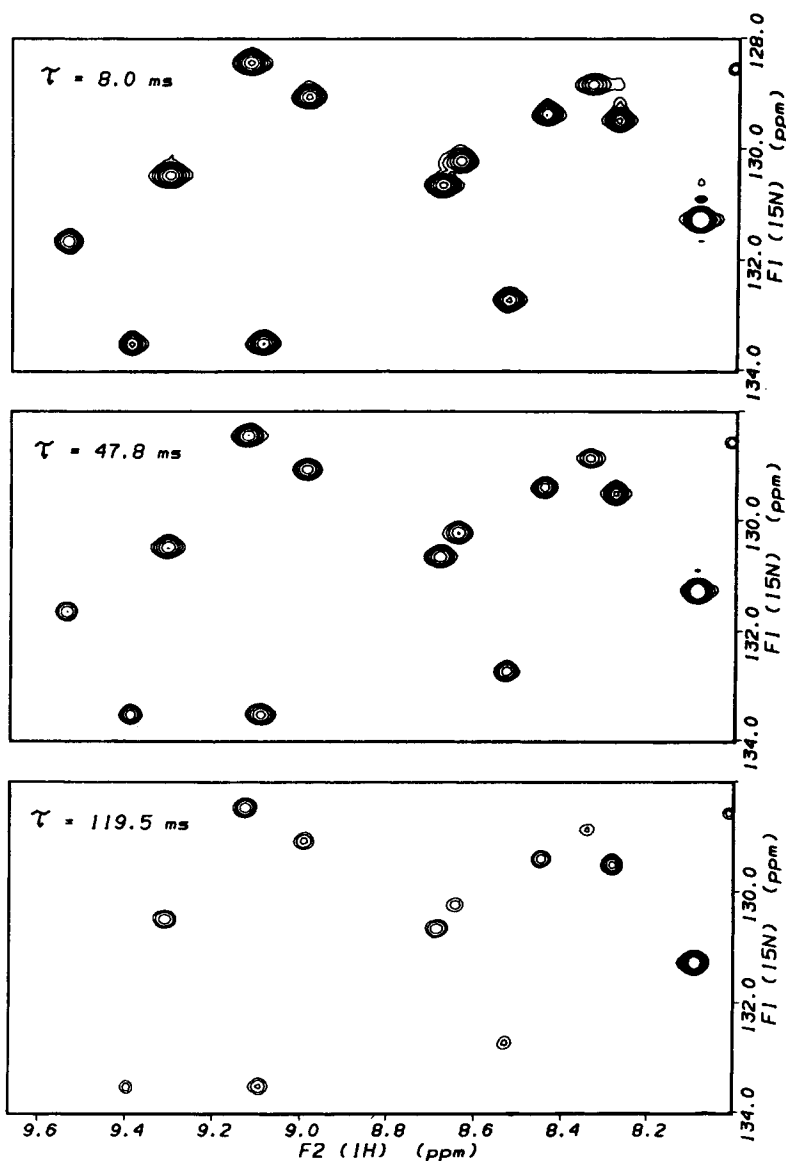


Fig. 4. Examples of 600 MHz 2D  $^1\text{H}$ - $^{15}\text{N}$  correlation spectra from which the  $^{15}\text{N}$   $T_2$  values have been derived. The CPMG delays ( $\tau$ ) are given in the upper left corners of each of the three example spectra. The region shown is the same as that displayed in Figure 2. Experimental conditions are given in the caption of Figure 1.

X-ray structures.<sup>16</sup> Residues involved in V<sub>L</sub>:V<sub>H</sub>, V<sub>L</sub>:digoxin, and crystal contacts are also indicated.

### $^1\text{H}$ - $^2\text{H}$ Exchange Rates

Figure 6 shows a spectral region containing most of the crosspeaks of interest regarding the  $^1\text{H}$ - $^2\text{H}$  exchange rates. Spectra with exchange delays of 34, 757, 4,026, and 22,736 min are displayed. Exchange rates were determined explicitly for 60 residues; these  $k_{\text{ex}}$  values range from  $(3.7 \pm 0.6) \times 10^{-6} \text{ min}^{-1}$  (Tyr-91) to  $\sim 3 \times 10^{-2} \text{ min}^{-1}$  (Gln-18). By reference to 2D homonuclear  $^1\text{H}$  NMR data, from which a qualitative assessment of backbone amide hydro-

gens in slow exchange has been reported,<sup>40</sup> a number of degenerate crosspeaks in the HSQC data could be assigned to specific residues. For example, a crosspeak appearing in the HSQC spectra which otherwise could involve Ile-21 and/or Arg-59 was assigned to the former residue based on the previous results.<sup>40</sup> Nevertheless, overlap prevents us from making an estimation of  $k_{\text{ex}}$  for nine residues. A lower limit on  $k_{\text{ex}}$  of  $\sim 3 \times 10^{-2} \text{ min}^{-1}$  is established for 33 residues. An upper limit on  $k_{\text{ex}}$  of  $\sim 2 \times 10^{-4} \text{ min}^{-1}$  is established for Gln-43. The  $^1\text{H}$ - $^{15}\text{N}$  crosspeak for Gln-43 persists up to an exchange delay of at least 11,223 min, but it is too weak at all



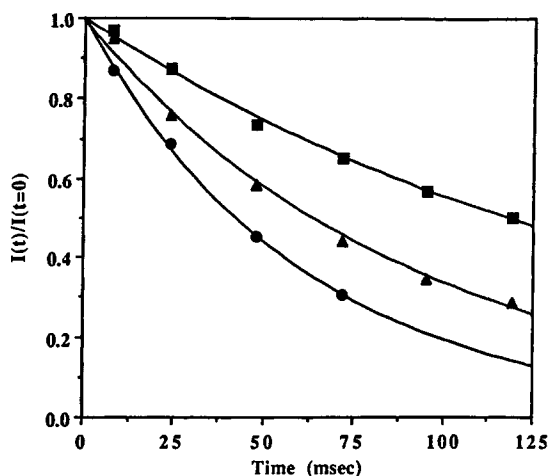


Fig. 5. Representative  $T_2$ -decay curves. Normalized experimental data points for Arg-113 ( $T_2 = 170 \pm 1$  ms), Leu-78 ( $T_2 = 93 \pm 2$  ms), and Gln-6 ( $T_2 = 61 \pm 3$  ms) are indicated by  $\blacksquare$ ,  $\blacktriangle$ , and  $\bullet$  symbols, respectively. The solid lines represent best-fit exponential decays to the experimental data.

exchange delay times to permit accurate peak height quantitation. This is probably due to short  $^1\text{H}$  and  $^{15}\text{N}$   $T_2$  values for this residue. Finally,  $k_{\text{ex}}$  for the Trp-40 sidechain  $\text{H}^1\text{N}$  proton has been determined to be  $(2.6 \pm 0.1) \times 10^{-5} \text{ min}^{-1}$ . The  $^1\text{H}$ - $^2\text{H}$  exchange data are described more fully in the Discussion section. The derived exchange rates, and their associated errors, are available in the Appendix.

## DISCUSSION

### Overall Rotational Correlation Time

As noted, an overall  $\tau_r$  of  $8.45 \pm 0.24$  ns has been determined. Similar  $\tau_r$  values were obtained for staphylococcal nuclease<sup>26</sup> (9.1 ns at 35°C, 1.5 mM protein) and interleukin-1 $\beta$ <sup>31</sup> (8.3 ns at 36°C, 2.0 mM protein), both of which are  $\sim 40$  to 50% larger than the 26-10  $V_L$  domain ( $\sim 17$  to 18 kDa versus  $\sim 12$  kDa, respectively). Minor  $V_L$  domain aggregation could account for an increase in the estimated  $\tau_r$ . The relatively large  $\tau_r$  of the  $V_L$  domain could also be due in part to differences in solvent viscosities reflecting the slightly higher temperatures and the lower protein concentrations employed in the staphylococcal nuclease and interleukin-1 $\beta$  studies. The hydrodynamic behavior of the  $V_L$  domain may be further influenced by the exposure of hydrophobic surface areas that are normally buried by  $V_L$ : $V_H$  association.<sup>54</sup> In addition, the overall  $V_L$  domain rotational motion may be slightly less isotropic than that of staphylococcal nuclease or interleukin-1 $\beta$ , as the principal components of the  $V_L$  domain inertial tensor, calculated from coordinates taken from the Fab structure,<sup>16</sup> have ratios of 1.62:1.57:1.00. Nevertheless, these ratios indicate that the degree of anisotropy of the overall  $V_L$  domain rotation is un-

likely to be large enough to invalidate an analysis based on a single  $\tau_r$ .<sup>38</sup> The appropriateness of the isotropic overall rotational model is confirmed by the large fraction (66%) of residues fit by Eq. (6), i.e., the relaxation data are well accounted for by a single overall rotational correlation time. Finally, we note that the staphylococcal nuclease and interleukin-1 $\beta$  studies were performed with pulse sequences which overestimate  $T_2$ ,<sup>27</sup> and hence underestimate  $\tau_r$ . In summary, the analysis of the relaxation data indicates that the 26-10  $V_L$  domain behaves in a reasonably isotropic manner and that it is predominantly monomeric under our experimental conditions.

### Dynamics on the ps–ns Timescale

A histogram showing the overall order parameter  $S^2$  for the 89 characterized residues is shown in Figure 7 (upper panel). For the 74 residues fit with Eq. (6) or Eq. (7),  $S^2$  values generally reflect the amplitudes of very fast ( $< 100$  ps) internal motions. The average value of  $S^2$  for these 74 residues is  $0.91 \pm 0.05$ , with high and low values of  $1.00 \pm 0.02$  (Asn-39) and  $0.72 \pm 0.07$  (Thr-96), respectively. The equivalent parameter for the 15 residues fit by Eq. (8) (two ps–ns internal motions) is  $S_f^2$ , which has an average value of  $0.87 \pm 0.04$ . Residues requiring Eq. (7) for an adequate fit to the data yielded an average fast internal correlation time  $\tau_e$  of  $45 \pm 27$  ps, with a high value of  $105 \pm 64$  (Glu-110) ps and a low value of  $12 \pm 11$  ps (Met-4). The  $\tau_e$  values are in general poorly defined, with the errors often exceeding 100%. This is typical for residues with high  $S^2$  and low  $\tau_e$  values,<sup>38</sup> as the contribution of the second term in Eq. (7) is relatively small for these cases. Residues fit by Eq. (6) very likely have internal correlation times  $< 20$  ps.

The striking feature of the  $S^2$  [residues fit by Eq. (6) or Eq. (7)] and  $S_f^2$  [residues fit by Eq. (8)] parameters is the uniformly high values obtained, which indicates uniformly low amplitudes for the very fast internal motions.<sup>31,55,56</sup> Results such as this typically reflect oscillations that occur within a single conformational substate,<sup>57</sup> i.e., within a local minimum on the free energy surface. The main contributions to this motion probably are  $\phi$  and  $\psi$  torsion angle fluctuations—librations of the amide planes—that do not involve barrier crossing.

A second class of fast internal motions is evidenced for the 15 residues fit by Eq. (8) (Table III). In all of these cases, attempts to fit  $T_1$  and  $T_2$  to Eq. (7) yielded parameters which predicted NOE values that were too small or negative. This reflects the high sensitivity of the NOE to the timescale of the motions.<sup>26</sup> The timescale for this class is considerably longer than that of the very fast motions discussed above. An average value of  $2.33 \pm 1.33$  ns for  $\tau_s$  [see Eq. (8)] has been determined, with a high value of  $6.49 \pm 1.24$  ns (Gly-73) and a low value of

TABLE I. NMR and X-Ray Data for Residues Fit by Eq. (6)

Residue	S <sup>2</sup>	R <sub>2ex</sub> (s <sup>-1</sup> )	B <sub>nat</sub> (Å <sup>2</sup> )	B <sub>comp</sub> (Å <sup>2</sup> )
Thr-5	0.87 ± 0.01	1.44 ± 0.06	10.5*	4.5 <sup>†</sup>
Gln-6	0.97 ± 0.01	4.44 ± 0.02	10.7	10.5 <sup>†</sup>
Thr-7	0.94 ± 0.01	2.04 ± 0.06	14.5	21.7 <sup>†</sup>
Leu-9	0.91 ± 0.01		11.0*	23.9 <sup>†</sup>
Leu-15	0.90 ± 0.01		8.7*	20.0 <sup>†</sup>
Gly-16	0.90 ± 0.01		10.4	19.8 <sup>†</sup>
Asp-17	0.97 ± 0.01		13.5	20.3
Gln-18	0.87 ± 0.01		14.1	24.2 <sup>†</sup>
Ser-20	0.86 ± 0.01		6.2	25.5
Ser-22	0.95 ± 0.01		12.2	11.7 <sup>†</sup>
Cys-23	0.92 ± 0.01	1.94 ± 0.06	11.4	15.3
Ser-25	0.96 ± 0.01	0.48 ± 0.20	13.2	13.0
Ser-26	0.94 ± 0.01	1.08 ± 0.24	15.9	15.6 <sup>†</sup>
Val-30	0.96 ± 0.01		10.8*	5.2
His-31	0.92 ± 0.02		10.3 <sup>‡</sup>	6.3 <sup>‡, **</sup>
Asn-33	0.99 ± 0.04		16.0*	8.8
Gly-34	0.90 ± 0.02		16.8*	2.0 <sup>†, ††</sup>
Asn-35	0.89 ± 0.01	1.80 ± 0.08	15.8*	7.7 <sup>†</sup>
Thr-36	0.86 ± 0.02	0.36 ± 0.17	15.3*	5.9
Tyr-37	0.84 ± 0.03		8.9 <sup>‡</sup>	5.3 <sup>‡</sup>
Leu-38	0.90 ± 0.03		8.9	2.0
Asn-39	1.00 ± 0.02		5.8 <sup>‡</sup>	6.1 <sup>‡, **</sup>
Trp-40	0.95 ± 0.01	4.56 ± 0.01	5.1	3.8
Tyr-41	0.92 ± 0.02		10.0 <sup>‡</sup>	2.0 <sup>‡, **</sup>
Gln-43	0.83 ± 0.05	4.08 ± 1.85	13.2 <sup>‡</sup>	9.6 <sup>‡</sup>
Lys-44	0.95 ± 0.02		16.4	19.4
Leu-52	0.95 ± 0.02		2.0	2.0
Ile-53	0.94 ± 0.02		2.0	11.5
Tyr-54	0.96 ± .01		3.8 <sup>*, ‡</sup>	11.1 <sup>†, ‡</sup>
Val-56	0.95 ± 0.02		4.9	11.3
Ser-57	0.85 ± 0.01	0.48 ± 0.19	4.6*	10.8 <sup>†</sup>
Asn-58	0.92 ± 0.01	1.80 ± 0.23	2.4*	15.0 <sup>†</sup>
Gly-62	0.83 ± 0.02		7.1	26.7
Val-63	0.87 ± 0.01	0.36 ± 0.14	8.2	19.3
Arg-66	0.93 ± 0.01		13.2	8.9
Phe-67	0.98 ± 0.01	0.72 ± 0.16	9.9	3.4

(continued)

TABLE I. NMR and X-Ray Data for Residues Fit by Eq. (6) (continued)

Residue	S <sup>2</sup>	R <sub>2ex</sub> (s <sup>-1</sup> )	B <sub>nat</sub> (Å <sup>2</sup> )	B <sub>comp</sub> (Å <sup>2</sup> )
Gly-69	0.91 ± 0.02		10.4*	9.9
Gly-71	0.88 ± 0.01		13.2*	8.8
Thr-74	0.92 ± 0.02		18.4	13.8 <sup>†</sup>
Asp-75	0.96 ± 0.02		16.5	14.7 <sup>†</sup>
Thr-77	0.92 ± 0.02		5.7	6.4 <sup>†</sup>
Ser-81	0.93 ± 0.01		13.3	17.0
Glu-84	0.89 ± 0.01	0.36 ± 0.14	18.0*	27.1 <sup>†</sup>
Ala-85	0.89 ± 0.01		17.7	23.8
Asp-87	0.90 ± 0.01	1.91 ± 0.01	11.0	13.9
Leu-88	0.96 ± 0.01		10.0	12.6
Ile-90	0.93 ± 0.01	0.48 ± 0.17	4.3 <sup>‡</sup>	14.6 <sup>‡</sup>
Tyr-91	0.93 ± 0.02		5.1	6.2
Phe-92	0.95 ± 0.01	1.20 ± 0.32	5.9 <sup>‡</sup>	10.7 <sup>‡</sup>
Cys-93	0.93 ± 0.02		8.4	7.8
Ser-94	0.95 ± 0.02		5.2	8.0 <sup>**</sup>
Thr-96	0.72 ± 0.07	7.56 ± 3.11	8.1 <sup>‡</sup>	10.4 <sup>‡, §, **</sup>
Thr-97	0.82 ± 0.01	1.56 ± 0.36	7.6	10.9
His-98	0.91 ± 0.01	0.84 ± 0.30	9.0	13.8 <sup>**</sup>
Gly-104	0.95 ± 0.01	5.28 ± 1.28	6.6	5.0
Gly-105	0.89 ± 0.01	4.08 ± 0.34	7.3 <sup>‡</sup>	8.9 <sup>‡</sup>
Gly-106	0.89 ± 0.01		7.3 <sup>‡</sup>	12.0 <sup>‡</sup>
Thr-107	0.91 ± 0.02		8.4	12.3
Leu-109	0.93 ± 0.02		11.1	12.8

\*Indicates residues with at least one atom (side chain or main chain) involved in crystal contacts (see Materials and Methods) in the native Fab X-ray structure.<sup>16</sup>

<sup>†</sup>Indicates residues with at least one atom (side chain or main chain) involved in crystal contacts in the digoxin complexed Fab X-ray structure.<sup>16</sup>

<sup>‡</sup>Indicates residues with at least one atom (side chain or main chain) involved in contacts with the V<sub>H</sub> domain in both the native and digoxin complexed Fab X-ray structure.<sup>16</sup>

<sup>§</sup>Indicates residues with at least one atom (side chain or main chain) involved in contacts with digoxin in the X-ray structure of the Fab/digoxin complex.<sup>16</sup>

<sup>\*\*</sup>Indicates residues with at least one atom (side chain or main chain) with surface area buried by digoxin (see Materials and Methods) in the X-ray structure of the Fab/digoxin complex.<sup>16</sup>

<sup>††</sup>2.0 Å<sup>2</sup> is the minimum possible B value by our methods.

0.81 ± 0.46 ns (Ala-45). Similar results have been obtained for subsets of interleukin-1β,<sup>31</sup> glucose permease IIA domain,<sup>3</sup> and calbindin D<sub>9k</sub><sup>35</sup> residues. These motions most likely represent a class of thermally activated barrier crossings, i.e., they may represent a low barrier tier in the hierarchy of transitions among conformational substates<sup>57</sup> involving the backbone NH groups.

The amplitudes of the ns timescale motions generally appear to be relatively low, as indicated by an average value of S<sub>s</sub><sup>2</sup> of 0.85 ± 0.13. A rough estimate of the fluctuation amplitudes can be obtained from a simple motional model which assumes that the NH vector jumps between two equally populated orientations separated by an angle φ<sub>s</sub>. This yields<sup>31</sup>

$$S_s^2 = (1 + 3 \cos^2 \phi_s)/4. \quad (10)$$

The derived values of φ<sub>s</sub> are displayed in Figure 7 (second panel). The average φ<sub>s</sub> value is 25 ± 11°. Only four residues display φ<sub>s</sub> > 30°; these are Gly-46 (φ<sub>s</sub> = 35°), Gly-73 (φ<sub>s</sub> = 45°), Lys-112 (φ<sub>s</sub> = 36°), and Arg-113 (φ<sub>s</sub> = 53°). The latter two residues are at the C-terminal end of the protein. Gly-46 is in a turn connecting β-strands C and C', and Gly-73 is in a turn connecting β-strands D and E. A stereoview of the V<sub>L</sub> domain backbone derived from the X-ray data<sup>16</sup> is shown in Figure 8. Residues displaying ns timescale motions are depicted in yellow. We note that additional residues may also have ns timescale motions which are obscured by exchange contributions to R<sub>2</sub> (discussed below), since, as previously mentioned, we do not have sufficient data to characterize two (timescale-separated) ps–ns motions and one μs–ms motion simultaneously. A residue that may display such complicated dynamic behav-

TABLE II. NMR and X-Ray Data for Residues Fit by Eq. (7)

Residue	$S^2$	$\tau_e$ (ps)	$R_{2ex}$ ( $s^{-1}$ )	$B_{nat}$ ( $\text{\AA}^2$ )	$B_{comp}$ ( $\text{\AA}^2$ )
Val-3	$0.90 \pm 0.01$	$56 \pm 16$	$1.20 \pm 0.23$	12.3*	5.3 <sup>†</sup>
Met-4	$0.89 \pm 0.01$	$12 \pm 11$	$0.72 \pm 0.16$	10.4	2.0
Val-13	$0.93 \pm 0.02$	$14 \pm 47$		12.1	19.1
Arg-24	$0.91 \pm 0.01$	$21 \pm 1$	$3.36 \pm 0.01$	10.6	13.5 <sup>†</sup>
Gln-27	$0.93 \pm 0.02$	$35 \pm 70$		15.4	20.2 <sup>†</sup>
Leu-29	$0.91 \pm 0.04$	$90 \pm 120$		9.1	8.7
Ser-32	$0.95 \pm 0.01$	$41 \pm 56$	$0.72 \pm 0.21$	13.9	12.9
Gln-47	$0.94 \pm 0.02$	$65 \pm 91$		17.9	17.4
Ser-48	$0.89 \pm 0.01$	$56 \pm 1$	$4.20 \pm 0.01$	12.3 <sup>‡</sup>	19.0 <sup>‡</sup>
Lys-50	$0.89 \pm 0.01$	$41 \pm 10$	$2.76 \pm 0.21$	6.4	14.0
Ser-61	$0.79 \pm 0.01$	$18 \pm 1$	$6.00 \pm 0.01$	5.8	21.8
Arg-82	$0.89 \pm 0.02$	$35 \pm 43$		16.5*	18.8 <sup>†</sup>
Glu-86	$0.91 \pm 0.01$	$65 \pm 37$		16.6	18.5
Glu-110	$0.90 \pm 0.02$	$105 \pm 64$		10.3	10.1
Ile-111	$0.88 \pm 0.01$	$22 \pm 29$		10.5	14.3

\*See footnote (\*) of Table I.

<sup>†</sup>See footnote (†) of Table I.<sup>‡</sup>See footnote (‡) of Table I.

TABLE III. NMR and X-Ray Data for Residues Fit by Eq. (8)

Residue	$S_F^2$	$S_N^2$	$\tau_a$ (ns)	$B_{nat}$ ( $\text{\AA}^2$ )	$B_{comp}$ ( $\text{\AA}^2$ )
Val-2	$0.86 \pm 0.02$	$0.92 \pm 0.03$	$2.51 \pm 1.50$	16.9	8.9
Ser-10	$0.88 \pm 0.01$	$0.90 \pm 0.01$	$2.14 \pm 0.52$	12.0	16.0
Leu-11	$0.89 \pm 0.01$	$0.91 \pm 0.02$	$1.83 \pm 0.78$	14.6	3.0
Ala-19	$0.91 \pm 0.02$	$0.94 \pm 0.02$	$1.14 \pm 0.56$	8.8	23.6
Ala-45	$0.88 \pm 0.01$	$0.93 \pm 0.01$	$0.81 \pm 0.46$	19.7	26.2
Gly-46	$0.80 \pm 0.02$	$0.75 \pm 0.03$	$2.14 \pm 0.94$	20.3	21.0
Leu-51	$0.89 \pm 0.04$	$0.96 \pm 0.01$	$1.56 \pm 0.08$	8.4*	7.9*
Phe-60	$0.90 \pm 0.02$	$0.95 \pm 0.03$	$1.83 \pm 1.31$	3.4*	19.1*
Gly-73	$0.81 \pm 0.01$	$0.63 \pm 0.04$	$6.49 \pm 1.24$	20.4 <sup>†</sup>	6.3
Leu-78	$0.93 \pm 0.02$	$0.92 \pm 0.02$	$2.51 \pm 1.24$	7.8	2.9
Lys-79	$0.90 \pm 0.01$	$0.92 \pm 0.02$	$2.93 \pm 1.46$	9.5 <sup>†</sup>	13.6
Gly-89	$0.86 \pm 0.01$	$0.93 \pm 0.01$	$2.94 \pm 1.12$	9.0	14.8
Lys-108	$0.86 \pm 0.01$	$0.85 \pm 0.02$	$3.44 \pm 1.27$	9.9	14.2
Lys-112	$0.87 \pm 0.02$	$0.75 \pm 0.01$	$1.85 \pm 0.49$	15.1	12.7
Arg-113	$0.79 \pm 0.02$	$0.52 \pm 0.01$	$0.88 \pm 0.10$	13.0	13.0

\*See footnote (‡) of Table I.

<sup>†</sup>See footnote (\*) of Table I.

ior is Thr-96 (part of CDR3), which has a  $T_1$  value (893 ms) more than four standard deviations above the mean  $T_1$  ( $700 \pm 40$  ms), but has a  $T_2$  value (61 ms) nearly two standard deviations below the mean  $T_2$  ( $88 \pm 15$  ms). Another residue possibly displaying significant motion on both ps–ns and  $\mu$ s–ms timescales is Ser-61 (part of CDR 2), which has  $T_1 = 802$  ms and  $T_2 = 64$  ms.

In summary, the 26-10  $V_L$  domain appears to be rather rigid on the ps–ns timescale. The calculated order parameters, as well as the primary relaxation data (especially the paucity of low NOE values), demonstrate that this protein is relatively rigid on this fast timescale when compared to other proteins that have been characterized by detailed analysis of  $^{15}\text{N}$  relaxation measurements.<sup>26,31–35</sup>

### Dynamics on the $\mu$ s–ms Timescale

Motions on a slower timescale are evidenced by exchange contributions to  $R_2$ . These contributions are due to transitions among nuclear environments that have different chemical shifts. Although analytical expressions for  $R_{2ex}$  are available,<sup>38</sup> the extraction of accurate temporal information requires knowledge of the chemical shift differences between environments. Without this information, only approximate limits on the timescale of the motion can be established. The upper limit is comparable to the CPMG refocusing period ( $\sim 10^{-3}$  s).<sup>26</sup> The lower limit depends on the environment populations, the chemical shift differences, and the uncertainty in  $R_2$ . A reasonable estimate of the lower limit is  $\sim$

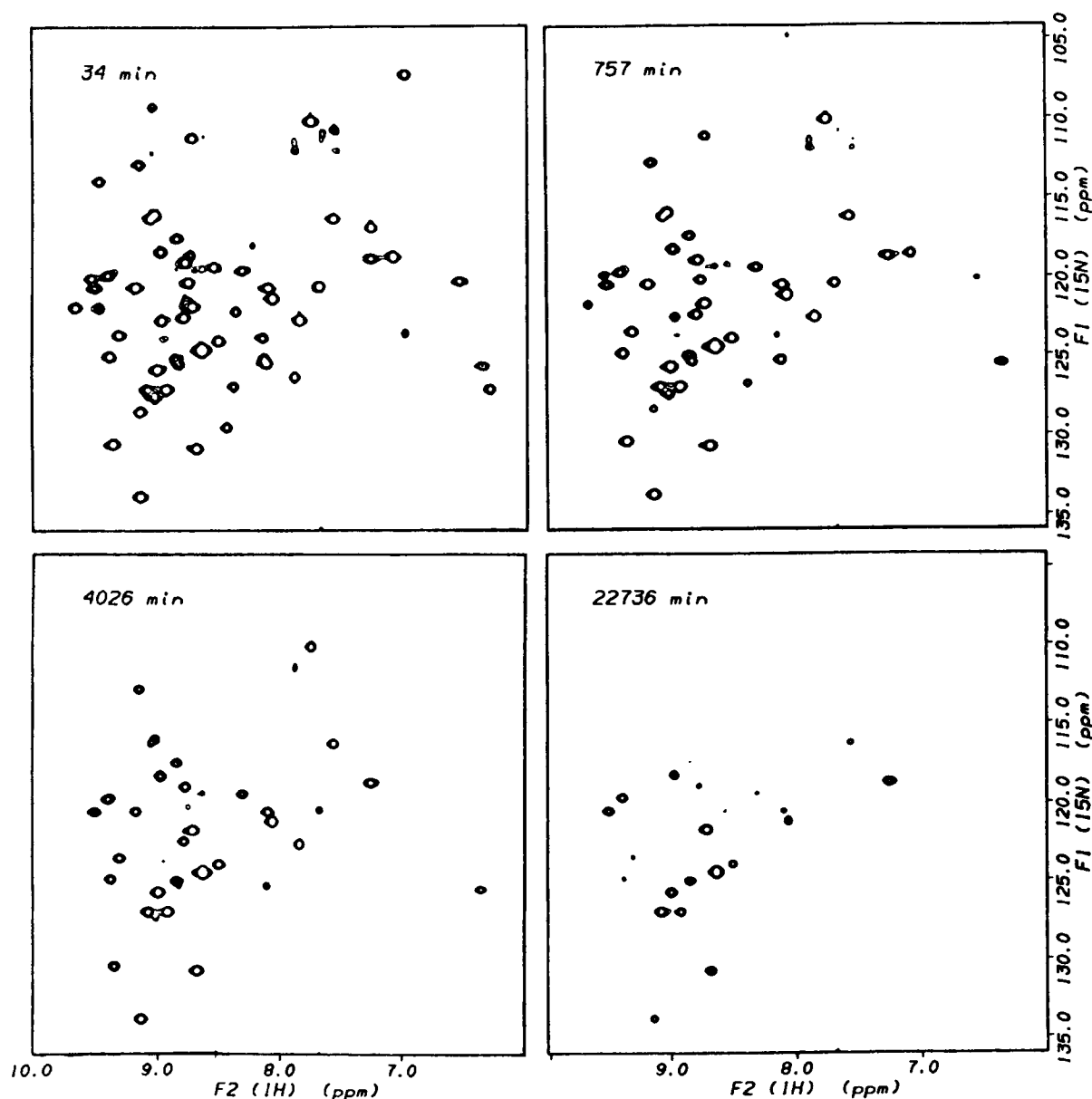


Fig. 6. Examples of 600 MHz 2D  $^1\text{H}$ - $^{15}\text{N}$  HSQC spectra from which the  $^1\text{H}$ - $^2\text{H}$   $k_{\text{ex}}$  values have been derived. The delays between dissolving the sample in  $^2\text{H}_2\text{O}$  and the midpoint of the experimental acquisition period are given in the upper left corners of each of the four example spectra. The spectra were recorded at 22°C on a 3.4 mM V<sub>L</sub> sample dissolved in 99.96%  $^2\text{H}_2\text{O}$  containing 50 mM deuterated NaOAc, 0.001%  $\text{NaN}_3$ , pH\* 5.5.

$10^{-6}$  s.  $R_2$  measurements will be insensitive to motions on this timescale if there is chemical shift degeneracy among the environments. We also note that, in general, NMR studies of protein dynamics in solution are “blind” to internal motions occurring on a timescale of  $\sim 10^{-8}$  to  $\sim 10^{-6}$  s.

The derived  $R_{2\text{ex}}$  values are shown in Figure 7 (third panel). Residues displaying significant exchange contributions to  $R_2$  are shown in red in Figure 8. Of particular interest are CDR residues dis-

playing such behavior. These are Ser-26, Ser-32, and Asn-35 of CDR1, Asn-58 and Ser-61 of CDR2, and Thr-96, Thr-97, and His-98 of CDR3. Thr-96 displays the largest  $R_{2\text{ex}}$  value of any residue ( $7.56 \text{ s}^{-1}$ ). This residue and Pro-101 are the only V<sub>L</sub> residues involved in extensive contacts with digoxin in the X-ray structure of the complex.<sup>16</sup> Other residues with significant  $R_{2\text{ex}}$  values include residues in turns (Ser-48, Phe-67, and Asp-87), residues in  $\beta$ -strand A (Val-3 through Thr-7), in  $\beta$ -strand B (Cys-

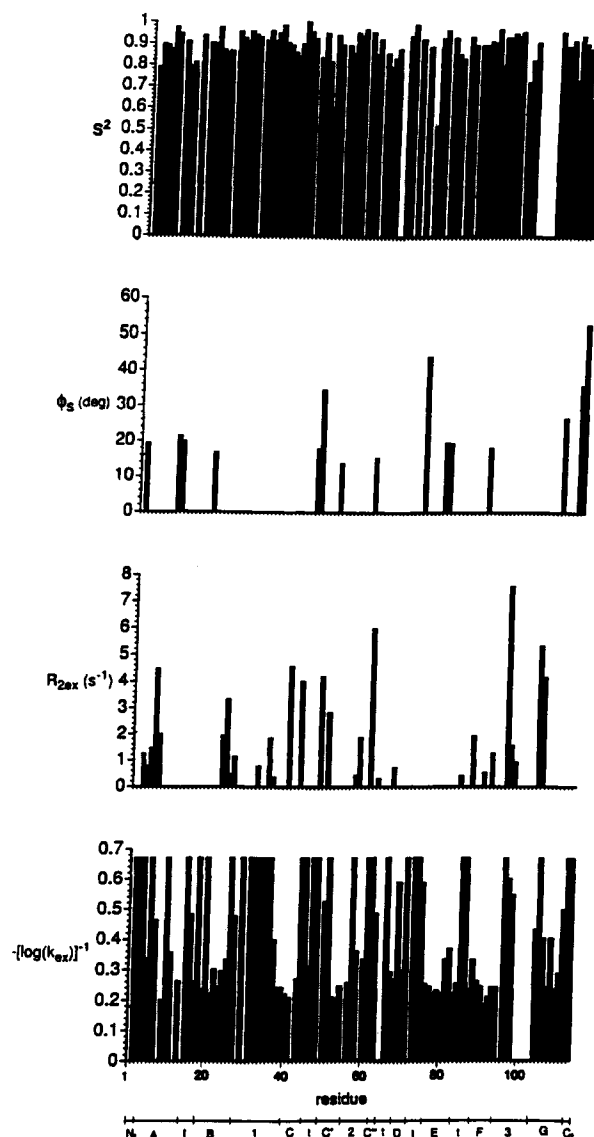


Fig. 7. Histograms summarizing the NMR-derived dynamic information for the 26-10  $V_1$  domain backbone HN groups. The upper diagram shows the total generalized order parameter  $S^2$  for 89 residues. [Note:  $S^2 = S_i^2 S_s^2$  for residues fit with Eq. (8).] The second diagram from the top shows  $\phi_s$  values (see text) for residues fit with Eq. (8). The third diagram displays the exchange contributions to  $R_2$  for 30 residues. Reciprocals of the negative logarithms of the  $^1\text{H}$ - $^2\text{H}$  exchange rates ( $\text{min}^{-1}$ ) for 94 residues are shown in the lower diagram. For this latter diagram, a value of 0.67 indicates a lower limit on  $k_{\text{ex}}$  of  $\sim 3 \times 10^{-2} \text{ min}^{-1}$ . All diagrams show a value of 0 for residues which were not characterized. Residue numbers are displayed along the horizontal axis of the lower diagram. At the very bottom, regions of the sequence corresponding to the N-terminus ( $N_t$ ), the C-terminus ( $C_t$ ), turns (t), CDRs (numbers), and  $\beta$ -strands (capital letters) are indicated.

23, Arg-24, and Ser-26), in  $\beta$ -strand C (Trp-40 and Gln-43), in  $\beta$ -strand C' (Lys-50), in  $\beta$ -strand F (Phe-92), and in the bulge feature<sup>54</sup> of  $\beta$ -strand G (Gly-104 and Gly-105).

There are a number of physical processes that can

produce exchange contributions to  $R_2$ . Loops may be involved in equilibria between distinct conformers. The NH groups in turns and loops may undergo transitions between significantly populated sub-states distinguished by amide plane rotations or by formed and broken hydrogen bonds. Such events have been observed in cyclic peptides;<sup>58,59</sup> it is likely that the more flexible regions of proteins can also display this behavior. Dynamic behavior other than motion of the NH vector *per se* is yet another factor to be considered. In particular, proximity to reorienting aromatic side chains will produce varying chemical shifts even at rigid NH sites. This mechanism provides a possible explanation for those residues, e.g., Trp-40, that show both exchange contributions to  $R_2$  and slow  $^1\text{H}$ - $^2\text{H}$  exchange. Proximity to transiently bound  $\text{H}_2\text{O}$  may contribute to transverse relaxation.<sup>31</sup> These issues are discussed more fully with reference to the X-ray data (see below). We note that the H3 loop of the antidansyl antibody studied by Arata and co-workers,<sup>39</sup> for which all residues were found to have unusually low  $T_2$  values (15–40 ms) in the absence of hapten, contains eight aromatic residues. In such a case, it is difficult to disentangle the relative contributions to  $R_2$  of the backbone motions from the motions of the aromatic rings.

#### Fluctuations Leading to $^1\text{H}$ - $^2\text{H}$ Exchange

A histogram of  $-\log(k_{\text{ex}})^{-1}$  is shown in Figure 7 (lower panel). Residues with  $k_{\text{ex}} > 3 \times 10^{-2} \text{ min}^{-1}$ , with  $3 \times 10^{-2} \text{ min}^{-1} \geq k_{\text{ex}} \geq 3 \times 10^{-4} \text{ min}^{-1}$ , and with  $k_{\text{ex}} < 3 \times 10^{-4} \text{ min}^{-1}$  are displayed in yellow, red, and blue, respectively, in Figure 9. Regions of the sequence showing extensive stretches of slowly exchanging NH protons include the major parts of  $\beta$ -strands B, C, E, and F. CDR2 and  $\beta$ -strands A, C', D, and G display mixed behavior, while  $\beta$ -strand C'', CDR1, CDR3, and most turn residues are predominantly characterized by fast exchange. There is a tendency for the loops, turns, and chain-terminal regions to show both faster hydrogen exchange and enhanced relaxation-active motions, but many residues lack correlation between their hydrogen exchange and relaxation data. Residues exhibiting significant ps–ns motions may display relatively fast exchange (e.g., Gly-73,  $k_{\text{ex}} > 3 \times 10^{-2} \text{ s}^{-1}$ ) or relatively slow exchange (e.g., Gly-46,  $k_{\text{ex}} = 5.8 \times 10^{-4} \text{ s}^{-1}$ ). An analogous situation holds for residues displaying exchange contributions to  $R_2$ . The inconsistencies among the hydrogen exchange and relaxation data must be considered with regard to the actual processes that hydrogen exchange rates are likely to reflect.

Models of internal motions which lead to the exchange of labile hydrogens have been detailed elsewhere.<sup>60,61</sup> During the exchange event, the NH must be accessible to an exchange catalyst ( $\text{OH}^-$  under our conditions) and must not be involved in

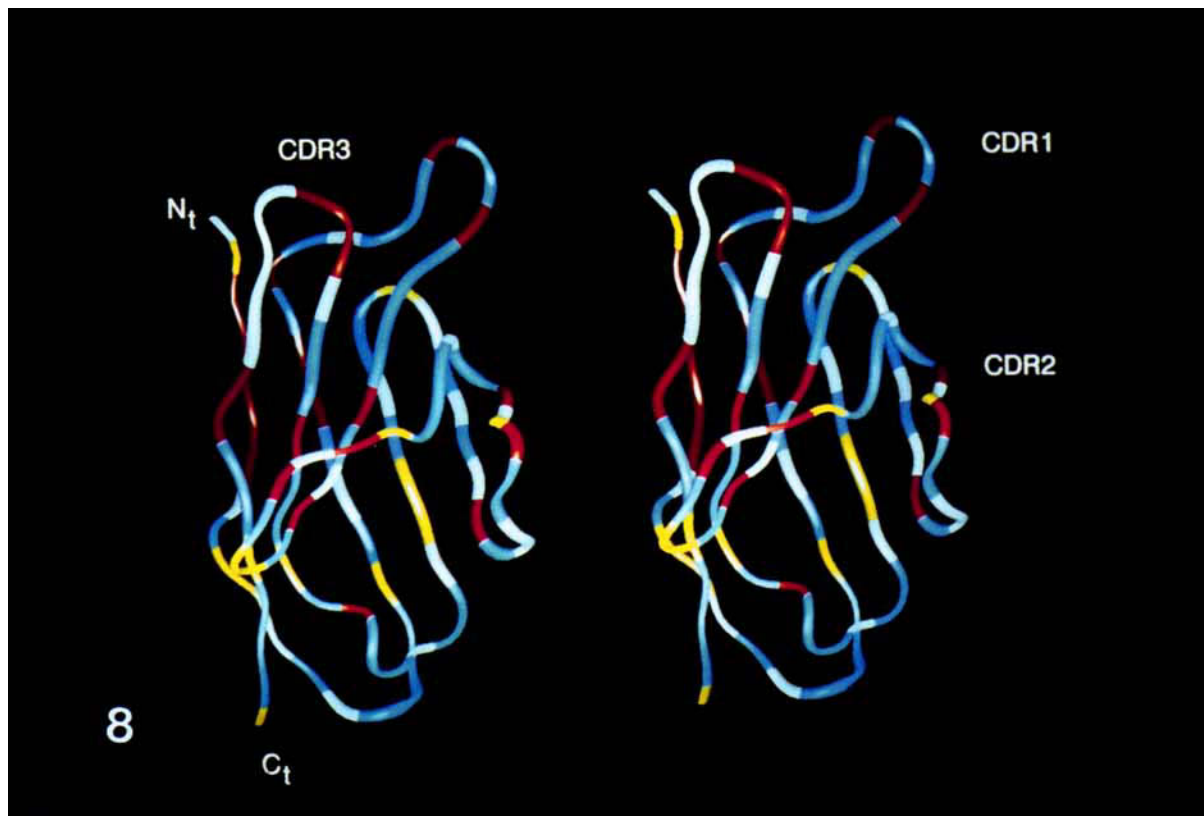


Fig. 8. Stereoview of the 26-10  $V_L$  domain polypeptide backbone derived from X-ray data—mapping of relaxation data. The C-terminus, the N-terminus, and the CDRs are labeled. Residues showing ns timescale motions are shown in yellow, and residues with significant exchange contributions to  $R_2$  are shown in red. The remaining residues characterized by the relaxation data are shown in blue, and uncharacterized residues are shown in shadowed white. Arg-113 is not shown.

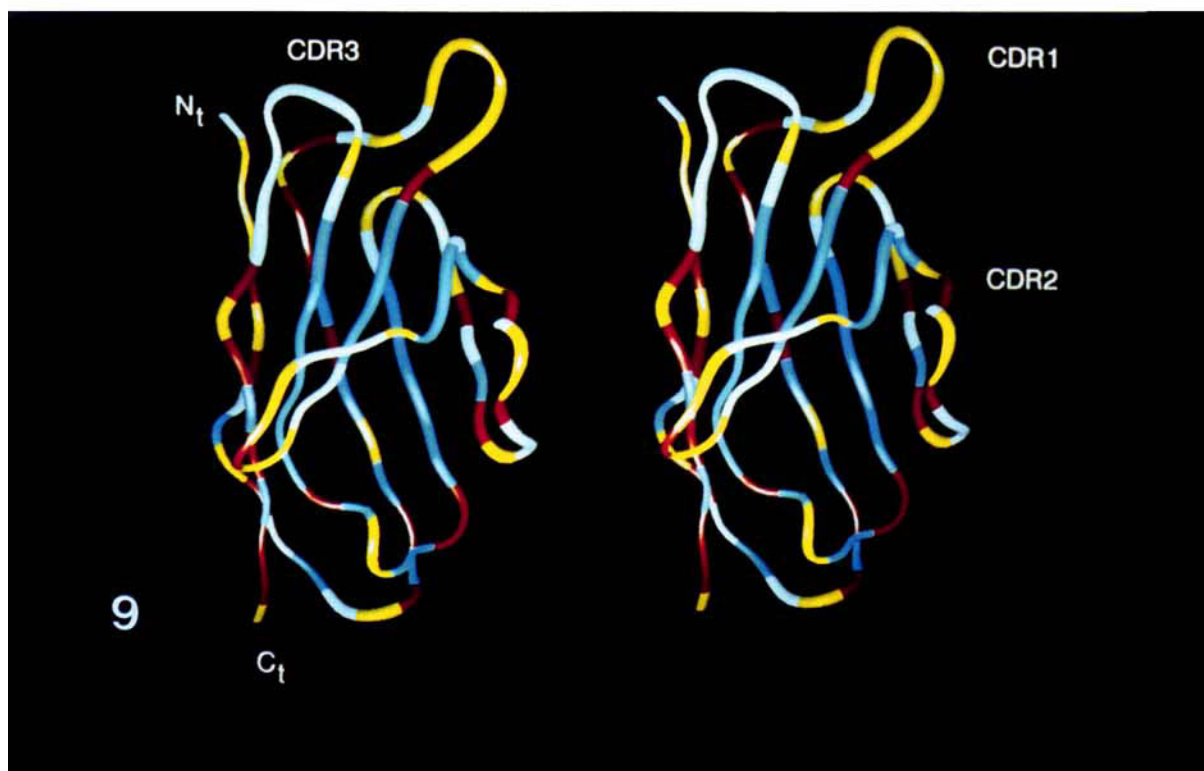


Fig. 9. Stereoview of the 26-10  $V_L$  domain polypeptide backbone derived from X-ray data—mapping of  $^1\text{H}$ - $^2\text{H}$  exchange data. The C-terminus, the N-terminus, and the CDRs are labeled. Residues with  $k_{\text{ex}} > 3 \times 10^{-2} \text{ min}^{-1}$  are shown in yellow, those with  $3 \times 10^{-2} \text{ min}^{-1} \geq k_{\text{ex}} \geq 3 \times 10^{-4} \text{ min}^{-1}$  are shown in red, and those with  $k_{\text{ex}} < 3 \times 10^{-4} \text{ min}^{-1}$  are displayed in blue. Uncharacterized residues are shown in shadowed white. Arg-113 is not shown.

intramolecular hydrogen bonding. At temperatures well below the thermal melting midpoint ( $\sim 55^\circ\text{C}$  for the 26-10  $V_L$  domain<sup>40</sup>), two general processes may allow otherwise protected hydrogens to exchange. These are described by the solvent penetration model,<sup>62</sup> wherein exchange catalysts migrate through transient cavities into the protein interior, and by the local unfolding model,<sup>63</sup> wherein local structural elements transiently unfold. Evidence<sup>64</sup> suggests that the former model is more appropriate for highly flexible regions of proteins, while the latter better describes exchange in regions of enhanced stability. With the possible exception of highly exposed non-hydrogen-bonded NH groups, hydrogen exchange rates reflect fluctuations into rare, high-energy conformers. This is a fundamental difference between hydrogen exchange and relaxation data, as the latter are sensitive only to transitions between well-populated substates. (Slow motions on the chemical shift timescale between well populated substates would be evidenced by multiple resonances, which are not observed for the backbone NH groups of the 26-10  $V_L$  domain.) Thus, regardless of the model, hydrogen exchange rates provide a measure of *local structural softness*. Perhaps most importantly, relatively fast rates indicate regions that may tolerate significant changes in their time-averaged conformations in response to external perturbations. These regions may or may not exist in one predominant conformational substate, and those that do exist in multiple substates may still show reduced hydrogen exchange rates if the hydrogens remain protected. In general, hydrogen exchange rates are expected to correlate with both hydrogen bonding and burial from the solvent.<sup>65</sup> These issues are examined below.

### Dynamic Information From X-Ray Data

X-ray crystallography provides information on the time-average positions of the heavy atoms in a protein crystal. These data allow dynamic information from various sources to be correlated with specific structural features. In addition, X-ray diffraction provides information on the spatial extent of protein motions.<sup>66</sup> The Debye–Waller model<sup>67</sup> relates the crystallographic  $B$ -factor (or Debye–Waller factor) to the mean-square radial atomic displacement  $\langle r^2 \rangle$  by

$$B = 8\pi^2 \langle r^2 \rangle / 3. \quad (11)$$

This model assumes isotropic, independent atomic fluctuations, and it does not easily distinguish the contributions of static disorder and whole-protein rigid-body movements in the crystal from internal dynamics.<sup>68</sup> Furthermore, it is now well established that crystal contacts can significantly alter a protein's dynamical spectrum from that pertaining to the solution state or to alternate crystal forms,<sup>65,69</sup>

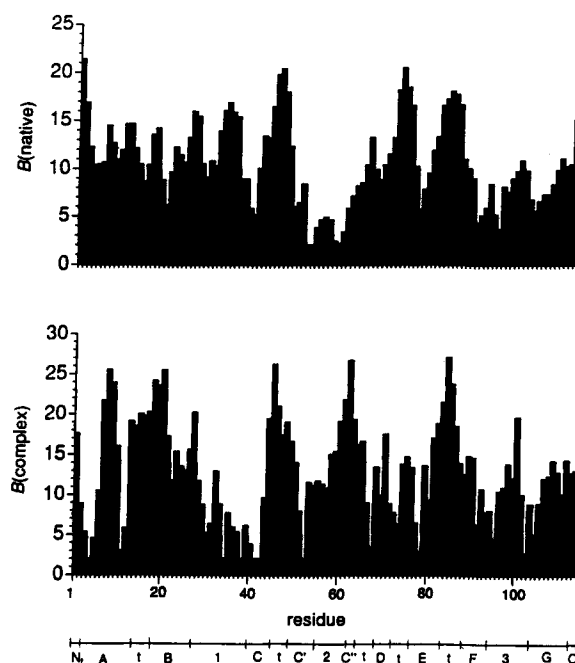


Fig. 10. Histograms summarizing isotropic  $B$ -factors ( $\text{\AA}^2$ ) for the  $V_L$  domain backbone N atoms within the native (upper diagram) and digoxin-complexed (lower diagram) X-ray structures. Residue numbers are displayed along the horizontal axis of the lower diagram. At the very bottom, regions of the sequence corresponding to the N-terminus (N), the C-terminus (C), turns (t), CDRs (numbers), and  $\beta$ -strands (capital letters) are indicated.

even at sites distant from the crystal contacts.<sup>65</sup> In the case of the 26-10  $V_L$  domain, contacts with the  $V_H$  domain and with digoxin may also alter the protein's dynamical spectrum. Despite these complications, it is worthwhile to compare both the structural and dynamic crystallographic information for the native and complexed Fab structures<sup>16</sup> to the solution dynamical information on the  $V_L$  domain. Before comparing the NMR and X-ray data, we briefly discuss the X-ray structures, including notable differences in the native and complex  $B$ -factors.

Figure 10 shows histograms of the  $V_L$  domain  $B$ -factors in the native (upper panel) and digoxin complexed (lower panel) Fab crystal structures. Figures 11 and 12 show  $B$ -factor ranges for the native and complexed structures, respectively, with regions of high, medium, and low  $B$ -factors indicated by yellow, red, and blue, respectively. Regions that appear to be relatively mobile in both structures include most of the stretch spanning the N-terminus through  $\beta$ -strand B, the turn connecting  $\beta$ -strands C and C', and the turn connecting  $\beta$ -strands E and F. Most of the region from CDR3 through the C-terminus displays medium to high  $B$ -factors. (Note that the "C-terminal" region in the Fab structures is not the end of the polypeptide chain, which in these cases extends to the flexible elbow region and the  $C_L$  domain.) Several major differences between the rel-

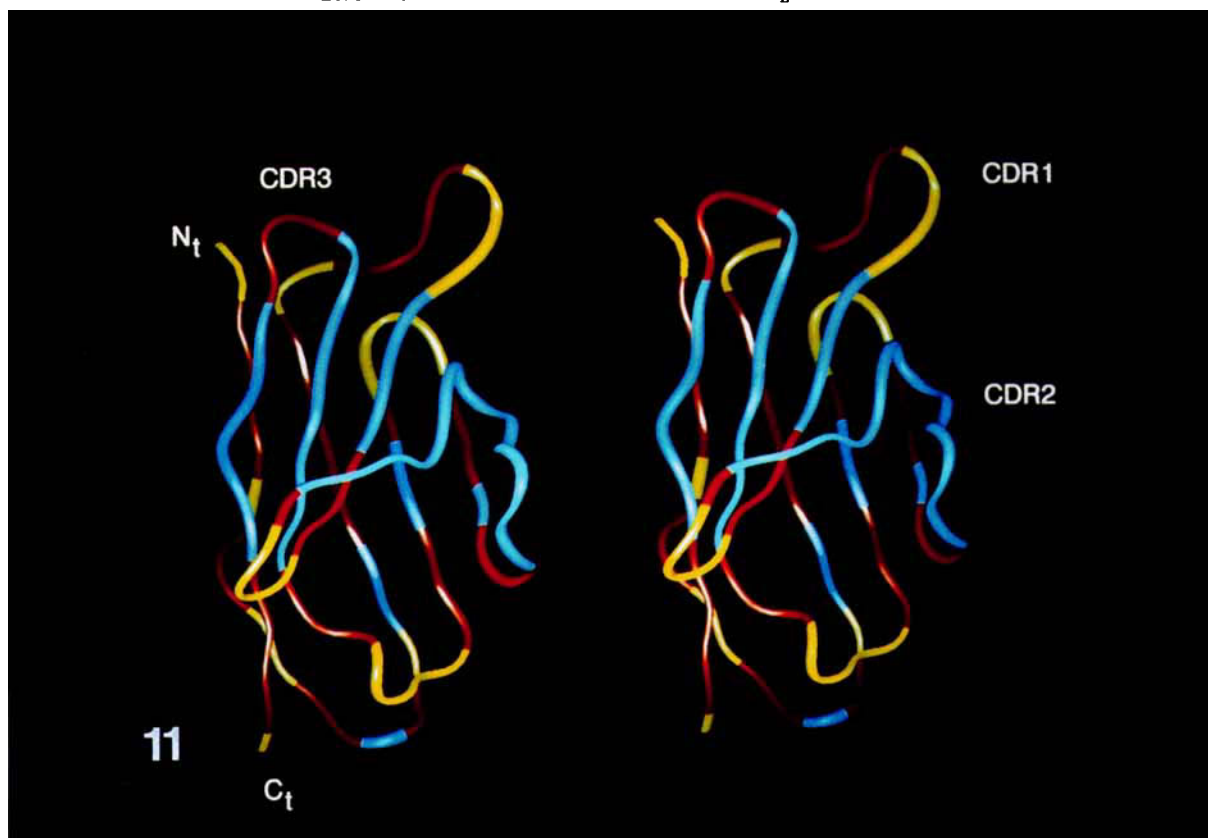


Fig. 11. Stereoview of the 26-10 V<sub>L</sub> domain polypeptide backbone derived from X-ray data—mapping of *B*-factors from the native Fab. The C-terminus, the N-terminus, and the CDRs are labeled. Residues with *B*-factors  $> 14 \text{ \AA}^2$  are shown in yellow, those with  $14 \text{ \AA}^2 \geq B \geq 9 \text{ \AA}^2$  are shown in red, and those with  $B < 9 \text{ \AA}^2$  are shown in blue. Arg-113 is not shown.

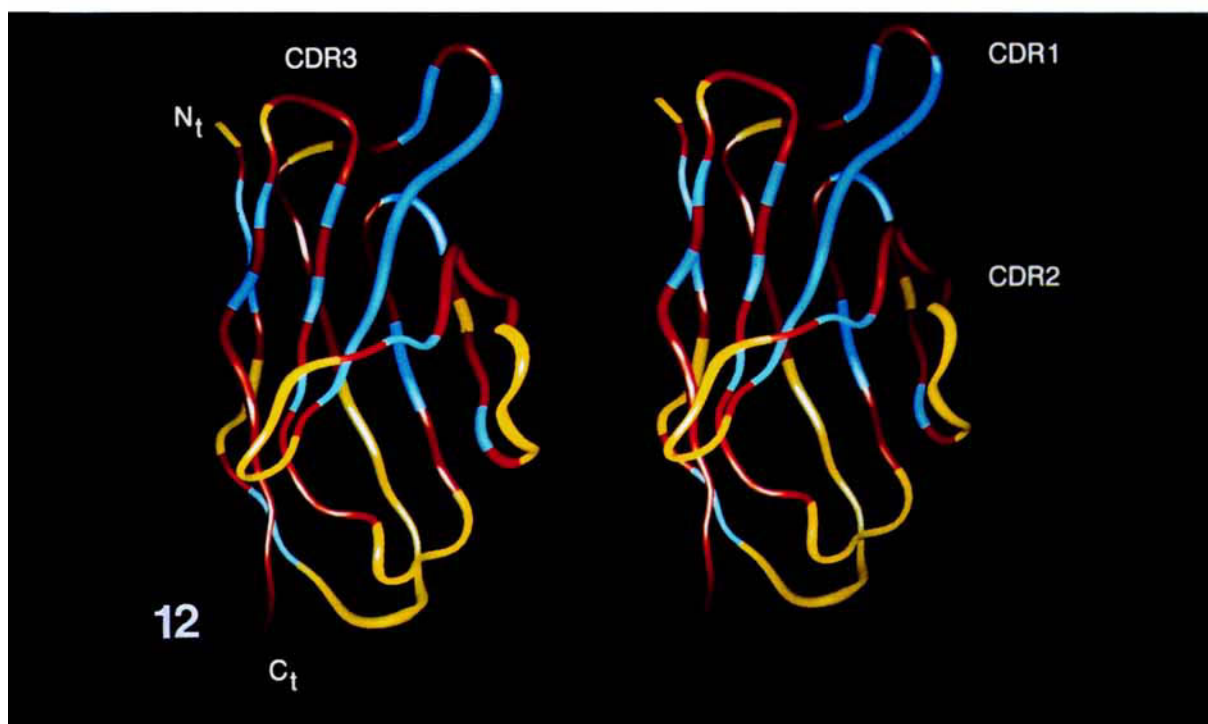


Fig. 12. Stereoview of the 26-10 V<sub>L</sub> domain polypeptide backbone derived from X-ray data—mapping of *B*-factors from the Fab/digoxin complex. The C-terminus, the N-terminus, and the CDRs are labeled. Residues with *B*-factors  $> 16 \text{ \AA}^2$  are shown in yellow, those with  $16 \text{ \AA}^2 \geq B \geq 8 \text{ \AA}^2$  are shown in red, and those with  $B < 8 \text{ \AA}^2$  are shown in blue. Arg-113 is not shown.



ative  $B$ -factors in the native and complexed Fab data are evident. (In general, the  $B$ -factors from a given structure refinement have reliable relative magnitudes; however, comparing the absolute  $B$ -factor magnitudes between different refinements is prone to error,<sup>66</sup> especially at moderate resolution.) Residues Ser-32 through Thr-36 (part of CDR1) and Gly-71 through Asp-75 comprise "spikes" of relatively high  $B$ -factors in the native Fab which are significantly reduced in the complex. The opposite effect is seen for the  $B$ -factor spike involving residues Asn-58 through Asp-65 (which includes most of CDR2 and  $\beta$ -strand C'') in the Fab/digoxin complex: its relative height is significantly reduced in the native Fab. These trends are not easily accounted for by an examination of direct contacts. Residues 34 and 35 are involved in crystal contacts in both structures. These residues do not participate in  $V_H$  domain contacts in either structure or in digoxin contacts in the complexed structure. Residues 71 through 75 also do not participate  $V_H$  or digoxin contacts, and residues in this region make crystal contacts in both the native and digoxin complexed forms. Residues 58 through 65 are not involved in digoxin contacts. Residue 58 is involved in extensive crystal contacts in both structures. Residue 60 is involved in  $V_L:V_H$  contacts in the native and digoxin complexed Fabs.

### Comparison of NMR and X-Ray Data

As with the NMR data, the crystallographic  $B$ -factors reveal an overall tendency for enhanced flexibility in the loops, turns, and terminal regions. Given the influence of  $V_L:V_H$  and  $V_L$ /digoxin contacts, the residue-specific NMR and crystallographic dynamic information may be expected to be even less correlated than what is observed in the interleukin-1 $\beta$  case.<sup>31</sup> Nevertheless, several interesting correlations are evident. The two residues outside the C-terminal region of the  $V_L$  domain which show relatively large amplitude ns motions (Gly-46 and Gly-73) also display the highest  $B$ -factors for non-terminal residues in the native Fab crystal structure. These are 20.3 and 20.4  $\text{\AA}^2$  for Gly-46 and Gly-73, respectively. While Gly-46 appears to remain relatively mobile in the digoxin complex ( $B = 21.0 \text{ \AA}^2$ ), Gly-73 appears to be immobilized upon complexation ( $B = 6.3 \text{ \AA}^2$ ). This is evidence of a reduction in motion at a location near, but not in direct contact with, the bound hapten.

The  $R_{2ex}$  data and the  $B$ -factors are not well correlated. The best correlation is observed for the regions of  $\beta$ -strands A and B showing exchange contributions to  $R_2$ , as these strands are characterized by medium to high  $B$ -factors. The two residues displaying the largest  $R_{2ex}$  values (Ser-61 and Thr-96) both have interesting  $B$ -factor properties. Thr-96 ( $R_{2ex} = 7.56 \text{ s}^{-1}$ ) has medium-low  $B$ -factors in both the native ( $B = 8.1 \text{ \AA}^2$ ) and complexed ( $B = 10.1 \text{ \AA}^2$ )

Fab structures. This residue is involved in both  $V_L:V_H$  and  $V_L$ /digoxin contacts. Thus, its mobility may be quenched relative to the isolated  $V_L$  domain by  $V_L:V_H$  interactions. Ser-61 ( $R_{2ex} = 6.00 \text{ s}^{-1}$ ) has a relatively low  $B$ -factor in the native structure ( $B = 5.8 \text{ \AA}^2$ ) but a relatively high  $B$ -factor ( $B = 21.8 \text{ \AA}^2$ ) in the complex. Although Ser-61 is in CDR2, which is involved in crystal contacts in both structures, this particular residue is not directly involved in  $V_L:V_H$ ,  $V_L$ /digoxin, or crystal contacts. This result supports the idea<sup>2,9</sup> that in some instances ligand binding may enhance, rather than reduce, a protein's flexibility at locations distant from the binding site.

As mentioned previously, exchange contributions to  $R_2$  may arise from processes other than internal motion of the NH vector itself. Of particular interest are those  $R_2$  exchange-active residues that show retarded  $^1\text{H}$ - $^2\text{H}$  exchange and that are involved in intramolecular H-bonds on the basis of the X-ray data (see the Appendix). These include Cys-23 and Arg-24 of  $\beta$ -strand B, Trp-40 and Gln-43 of  $\beta$ -strand C, and Phe-92 of  $\beta$ -strand F. In the X-ray structure of the Fab/digoxin complex, the backbone N atoms of all of these residues are within 5.0  $\text{\AA}$  of one or more aromatic rings. The Cys-23 N is near the rings of Trp-40 and Phe-76, and Arg-24 N is also near Phe-76. Besides its own side chain, the N atom of Trp-40 is also near the ring of Tyr-41. The Gln-43 N is near the Phe-92 ring, and the Phe-92 N is near its own side chain as well as the rings of Trp-40 and Tyr-91. We suggest that the  $R_2$  exchange contributions obtained for these residues may be due, at least in part, to motions of the nearby rings. These motions must be more complex than 180° ring flips of Phe or Tyr side chains; they must involve alternate packing arrangements of the rings. A number of  $V_L$  domain aromatic rings are normally involved in packing interactions at the  $V_L:V_H$  interface.<sup>54</sup> Absence of these interactions in the isolated 26-10  $V_L$  domain may enhance side chain flexibility throughout the protein. Exchange of bound  $\text{H}_2\text{O}$  molecules may also contribute to  $R_2$ ; however, the  $\text{H}_2\text{O}$  positions are not well enough defined by the current crystallographic data to afford a detailed analysis. We note that the buried Trp-40 side chain is likely to be associated with a buried  $\text{H}_2\text{O}$  molecule.<sup>40</sup> This raises the interesting possibility that Trp-40 side chain motion coupled to the dynamic behavior of a buried  $\text{H}_2\text{O}$  may influence the transverse relaxation of nearby atoms.

$^1\text{H}$ - $^2\text{H}$  exchange rates are expected to show a correlation with hydrogen bonding and distances of the amide proton to the solvent accessible surface ( $r_{surf}$ ).<sup>65</sup> Of the 94 characterized residues, 58 are involved in intramolecular hydrogen bonding interactions (see the Appendix). A summary of the  $k_{ex}$  and  $r_{surf}$  data for the hydrogen bonded and non-hydrogen-bonded residues is given in Table IV. A number of correlations are evident. The distributions of hydrogen-bonded and non-hydrogen-bonded residues

**TABLE IV. Correlations Among <sup>1</sup>H-<sup>2</sup>H Exchange, Hydrogen Bonding, and Distances to the Solvent Accessible Surface**

$r_{\text{surf}}$ range (Å)*	Total <sup>†</sup>	High $k_{\text{ex}}$ <sup>‡</sup>	Medium $k_{\text{ex}}$ <sup>§</sup>	Low $k_{\text{ex}}$ <sup>**</sup>
36 non-hydrogen-bonded residues				
< 1.00	20	16	3	1
1.00 to 1.99	7	5	1	1
2.00 to 2.99	6	1	4	1
3.00 to 3.99	2	0	0	2
4.00 to 4.99	0	0	0	0
> 5.00	1	0	0	1
58 hydrogen-bonded residues				
< 1.00	2	1	0	1
1.00 to 1.99	11	4	5	2
2.00 to 2.99	20	3	10	7
3.00 to 3.99	18	3	6	9
4.00 to 4.99	6	0	1	5
> 5.00	1	0	0	1

\*Range of distances of the backbone amide protons to the solvent accessible surface (see Materials and Methods).

<sup>†</sup>Total number of residues falling within the given  $r_{\text{surf}}$  range.

<sup>‡</sup>Number of residues with  $k_{\text{ex}} > 3 \times 10^{-2} \text{ min}^{-1}$ .

<sup>§</sup>Number of residues with  $3 \times 10^{-2} \text{ min}^{-1} > k_{\text{ex}} > 3 \times 10^{-4} \text{ min}^{-1}$ .

<sup>\*\*</sup>Number of residues with  $k_{\text{ex}} < 3 \times 10^{-4} \text{ min}^{-1}$ .

are distinct with respect to  $r_{\text{surf}}$ —the number of non-hydrogen-bonded residues decreases steadily with increasing  $r_{\text{surf}}$ , whereas the number of hydrogen-bonded residues peaks at intermediate  $r_{\text{surf}}$  values. The relative number of residues showing slow <sup>1</sup>H-<sup>2</sup>H exchange increases with increasing  $r_{\text{surf}}$  for both hydrogen-bonded and non-hydrogen-bonded residues; however, the <sup>1</sup>H-<sup>2</sup>H exchange behavior is distinct among these two classes. Although the non-hydrogen-bonded backbone amide HN groups account for only 38% of the characterized residues, they include 67% of the residues showing rapid exchange. Indeed, nearly half (48%) of the residues with  $k_{\text{ex}} > 3 \times 10^{-2} \text{ min}^{-1}$  are in the non-hydrogen-bonded subclass with  $r_{\text{surf}} < 1.00 \text{ Å}$ . While the hydrogen-bonded residues comprise 62% of the characterized residues, they include 81% of the residues with  $k_{\text{ex}} < 3 \times 10^{-4} \text{ min}^{-1}$ . It is clear that the <sup>1</sup>H-<sup>2</sup>H exchange behavior of the 26-10 V<sub>L</sub> domain follows the expected trends. Nevertheless, several residues display <sup>1</sup>H-<sup>2</sup>H exchange behavior that is difficult to explain. In particular, Leu-9 manifests a very low  $k_{\text{ex}}$  ( $9.8 \times 10^{-6} \text{ min}^{-1}$ ), yet its HN is only 0.65 Å from the solvent accessible surface (essentially the minimum possible distance by our method) and is not hydrogen bonded, i.e., by these criteria the Leu-9 HN is highly exposed. Unusual steric interactions may offer one possible explanation for this result. Anomalous cases underscore the importance of experimentally characterizing <sup>1</sup>H-<sup>2</sup>H exchange rates.

## CONCLUDING REMARKS

This study has provided insights into the backbone motions of the isolated 26-10 antibody V<sub>L</sub> domain in solution and has compared these data to crystallographic information for the native and digoxin-complexed Fab structures. All examined residues undergo high-frequency (ps timescale), low-amplitude motions, which most likely represent librations within discrete conformational substates. A subset of residues has been observed to undergo ns timescale motions (corresponding to conformational transitions involving relatively low free energy barriers) as evidenced by lack of fit of their relaxation data to a model-free spectral density function based on one internal correlation time. Residues belonging to a second subset are sensitive to transitions between well-populated substates on the  $\mu\text{s}$ -ms timescale (corresponding to relatively high free energy barriers) as evidenced by exchange contributions to  $R_2$ . Possible causes of this latter behavior, in addition to actual motion of the NH vector, have been considered. Rare conformational excursions have been characterized by <sup>1</sup>H-<sup>2</sup>H exchange rates. These rates reflect structural features observed crystallographically, particularly hydrogen bonding and the degree of burial.

Both the X-ray and NMR data reveal an overall trend toward enhanced flexibility in turns, loops, and C-terminal and N-terminal regions. However, many residues do not display correlations between the degrees of flexibility indicated by the relaxation data, hydrogen exchange rates, and  $B$ -factors. This is not surprising, considering the differences in timescales, amplitudes, and (in the case of the  $B$ -factors) environments involved. Potential changes in the dynamic behavior of the V<sub>L</sub> domain upon association with the V<sub>H</sub> domain and subsequent complexation with digoxin have been noted. As these observations were based on the  $B$ -factor data, it will be interesting to examine the dynamic behavior of the native and digoxin-complexed 26-10 Fv fragment<sup>41</sup> in solution. The time-averaged conformation of the 26-10 Fab changes little upon complexation with digoxin,<sup>16</sup> and it is likely that no major changes in the time-averaged conformation of the V<sub>L</sub> domain occur upon V<sub>L</sub>:V<sub>H</sub> association.<sup>40</sup> Dynamic information may be more sensitive to interactions than measures of the time-average structure.

Although the 26-10 V<sub>L</sub> domain does have regions of enhanced flexibility, it appears to be overall a relatively rigid protein on the ps-ns timescale. Since similar comprehensive studies of other antibody domains have not been reported to date, it is not possible to determine whether this is a general feature of antibody domains, or a specific feature of 26-10. A relatively rigid antibody would tend to minimize the conformational entropy loss associated with the binding of a rigid hapten and, as suggested

previously,<sup>40</sup> would produce higher unfavorable strain energies in cases of induced fit associations. These considerations may play a role in the relatively high stability of the 26-10 Fv<sup>41</sup> ( $V_L:V_H K_a > 10^7 \text{ M}^{-1}$ ) and the minimal amount of  $V_L:V_L$  association observed. There is no obvious explanation for the enhanced 26-10 Fv stability on the basis of comparison to buried polar and hydrophobic surfaces observed in the  $V_L:V_H$  interfaces of other antibodies (J. Novotny, personal communication.) Such issues can be rigorously addressed only when detailed descriptions of both the main chain and side chain dynamics of a variety of structurally characterized antibody domains and their complexes become available.

### ACKNOWLEDGMENTS

We thank Dr. Lewis Kay for providing a copy of reference 27 prior to its publication, and Dr. Jiri Novotny for discussions and information regarding  $V_L:V_H$  interfaces. The assistance of Dr. William Metzler in the production of the figures is gratefully acknowledged.

### REFERENCES

- Lumry, R., Gregory, R.B. Free-energy management in protein reactions: Concepts, complications, and compensation. In "The Fluctuating Enzyme." Welch, G.R., ed. New York: Wiley-Interscience, 1986: 1-190.
- Lumry, R., Gregory, R.B. Dynamical factors in protein-protein association. *J. Mol. Liquids* 42:113-144, 1989.
- Karplus, M., McCammon, J.A. Dynamics of proteins: Elements and function. *Annu. Rev. Biochem.* 53:263-300, 1983.
- Careri, G., Gratton, E. The statistical time correlation approach to enzyme action: The role of hydration. In "The Fluctuating Enzyme." Welch, G.R., ed. New York: Wiley-Interscience, 1986: 227-262.
- Gavish, B. Molecular dynamics and the transient strain model of enzyme catalysis. In "The Fluctuating Enzyme." Welch, G.R., ed. New York: Wiley-Interscience, 1986: 263-340.
- Somogyi, B., Damjanovich, S. A microenvironmental approach to enzyme dynamics. In "The Fluctuating Enzyme." Welch, G.R., ed. New York: Wiley-Interscience, 1986: 341-368.
- Frohlich, H. Coherence and the action of enzymes. In "The Fluctuating Enzyme." Welch, G.R., ed. New York: Wiley-Interscience, 1986: 421-450.
- Kraut, J. How do enzymes work? *Science* 242:533-540, 1988.
- Lumry, R. Mechanical force, hydration, and conformational fluctuations in enzymic catalysis. In "A Study of Enzymes," Vol. II. Kuby, S.A., ed. Boca Raton, FL: CRC Press, 1991: 3-81.
- Farnum, M.F., Madge, D., Howell, E.E., Hirai, J.T., Warren, M.S., Grimsley, J.K., Kraut, J. Analysis of hydride transfer and cofactor fluorescence decay in mutants of dihydrofolate reductase: Possible evidence for participation of enzyme molecular motions in catalysis. *Biochemistry* 30:11567-11579, 1991.
- Pain, R.H., Varley, P.G. Relation between stability, dynamics and enzyme activity in 3-phosphoglycerate kinases from yeast and *Thermus thermophilus*. *J. Mol. Biol.* 220: 531-538, 1991.
- Daggett, V., Schroder, S., Killman, P. Catalytic pathway of serine proteases: Classical and quantum mechanical calculations. *J. Am. Chem. Soc.* 113:8926-8935, 1991.
- Akke, M., Forsen, S., Chazin, W.J. Molecular basis for cooperativity in  $\text{Ca}^{2+}$  binding to calbindin  $\text{D}_{9k}$ :  $^1\text{H}$  nuclear magnetic resonance studies of  $(\text{Cd}^{2+})_1$ -bovine calbindin  $\text{D}_{9k}$ . *J. Mol. Biol.* 220:173-189, 1991.
- Karslake, C., Botuyan, M.V., Gorenstein, D.G.  $^{31}\text{P}$  NMR spectra of oligodeoxyribonucleotide duplex *lac* operator-repressor headpiece complexes: Importance of phosphate ester backbone flexibility in protein-DNA recognition. *Biochemistry* 30:1849-1858, 1992.
- Schultz, P.G., Benkovic, S.J., Lerner, R.A. At the crossroads of chemistry and immunology: Catalytic antibodies. *Science* 252:659-667, 1991.
- Jeffrey, P.D., Strong, R.K., Sieker, L.C., Chang, C.Y., Campbell, R.L., Petsko, G.A., Haber, E., Margolies, M.N., Sheriff, S. 26-10 Fab:digoxin complex—affinity and specificity from shape complementarity. Submitted 1992.
- Herron, J.N., He, X.M., Ballard, D.W., Bleir, P.R., Pace, P.E., Bothwell, A.L.M., Voss, E.W., Edmundson, A.B. An autoantibody to single-stranded DNA: Comparison of the three-dimensional structures of the unliganded Fab and a deoxynucleotide-Fab complex. *Proteins Struct. Funct. Genet.* 11:159-175, 1991.
- Rini, J.M., Schulze-Gahmen, U., Wilson, I.A. Structural evidence for induced fit as a mechanism for antibody-antigen recognition. *Science* 255:959-965, 1992.
- Davies, D.R., Sheriff, S., Padlan, E.A. Antibody-antigen complexes. *J. Biol. Chem.* 263:10541-10544, 1988.
- Colman, P.M. Structure of antibody-antigen complexes: Implications for immune recognition. *Adv. Immun.* 43:99-132, 1988.
- Bhat, T.N., Bentley, G.A., Fischman, T.O., Boulot, G., Poljak, R.J. Small rearrangements in structures of Fv and Fab fragments of antibody D1.3 on antigen binding. *Nature (London)* 347:483-485, 1990.
- Mueller, L., Ernst, R.R. Coherence transfer in the rotating frame: Application to heteronuclear cross-correlation spectroscopy. *Mol. Phys.* 38:963-992, 1979.
- Mueller, L. Sensitivity enhanced detection of weak nuclei using heteronuclear multiple quantum coherence. *J. Am. Chem. Soc.* 101:4481-4484, 1979.
- Bodenhausen, G., Ruben, D.J. Natural abundance nitrogen-15 NMR by enhanced heteronuclear spectroscopy. *Chem. Phys. Lett.* 69:185-188, 1980.
- Nirmala, N.R., Wagner, G. Measurement of  $^{13}\text{C}$  relaxation times in proteins by two-dimensional heteronuclear  $^1\text{H}$ - $^{13}\text{C}$  correlation spectroscopy. *J. Am. Chem. Soc.* 110:7557-7558, 1988.
- Kay, L.E., Torchia, D.A., Bax, A. Backbone dynamics of proteins as studied by  $^{15}\text{N}$  inverse detected heteronuclear NMR spectroscopy: Application to staphylococcal nuclease. *Biochemistry* 28:8972-8979, 1989.
- Kay, L.E., Nicholson, L.K., Delaglio, F., Bax, A., Torchia, D.A. Pulse sequences for the removal of the effects of cross-correlation between dipolar and chemical shift anisotropy relaxation mechanisms on the measurement of heteronuclear  $T_1$  and  $T_2$  values in proteins. *J. Magn. Reson.* 97: 359-375, 1992.
- Lipari, G., Szabo, A. Model-free approach to the interpretation of nuclear magnetic resonance relaxation in macromolecules. 1. Theory and range of validity. *J. Am. Chem. Soc.* 104:4546-4559, 1982.
- Lipari, G., Szabo, A. Model-free approach to the interpretation of nuclear magnetic resonance relaxation in macromolecules. 2. Analysis of experimental results. *J. Am. Chem. Soc.* 104:4559-4570, 1982.
- Clore, G.M., Szabo, A., Bax, A., Kay, L.E., Driscoll, P.C., Gronenborn, A.M. Deviations from the simple two-parameter model-free approach to the interpretation of nitrogen-15 nuclear magnetic relaxation in proteins. *J. Am. Chem. Soc.* 112:4989-4991, 1990.
- Clore, G.M., Driscoll, P.C., Wingfield, P.T., Gronenborn, A.M. Analysis of the backbone dynamics of interleukin-1 $\beta$  using inverse detected heteronuclear  $^{15}\text{N}$ - $^1\text{H}$  NMR spectroscopy. *Biochemistry* 29:7387-7401, 1990.
- Schneider, D.M., Dellwo, M.J., Wand, A.J. Fast internal main-chain dynamics of human ubiquitin. *Biochemistry* 31:3645-3652, 1992.
- Stone, M.J., Fairbrother, W.J., Palmer, A.G. III, Reizer, J., Saier, M.H. Jr., Wright, P.E. Backbone dynamics of the *Bacillus subtilis* glucose permease IIA domain determined from  $^{15}\text{N}$  NMR relaxation measurements. *Biochemistry* 31:4394-4406, 1992.

34. Barbato, G., Ikura, M., Kay, L.E., Pastor, R.W., Bax, A. Backbone dynamics of clamodulin studied by <sup>15</sup>N relaxation using inverse detected two-dimensional NMR spectroscopy: The central helix is flexible. *Biochemistry* 31: 5269–5278, 1992.
35. Kordel, J., Skelton, N.J., Akke, M., Palmer, A.G. III, Chazin, W.J. Backbone dynamics of calcium-loaded calbindin D<sub>9k</sub> studied by two-dimensional proton-detected <sup>15</sup>N NMR spectroscopy. *Biochemistry* 31:4856–4866, 1992.
36. Peng, J.W., Wagner, G. Mapping of spectral density functions using heteronuclear NMR relaxation measurements. *J. Magn. Reson.* 98:308–332, 1992.
37. Nicholson, L.K., Kay, L.E., Baldissieri, D.M., Arango, J., Young, P.E., Bax, A., Torchia, D.A. Dynamics of methyl groups in proteins as studied by proton-detected <sup>13</sup>C NMR spectroscopy. Application to the leucine residues of staphylococcal nuclease. *Biochemistry* 31:5253–5263, 1992.
38. Palmer, A.G. III, Rance, M., Wright, P.E. Intramolecular motions of a zinc finger DNA-binding domain from Xfin characterized by proton-detected natural abundance <sup>13</sup>C heteronuclear NMR spectroscopy. *J. Am. Chem. Soc.* 113: 4371–4380, 1991.
39. Takahashi, H., Suzuki, E., Shimada, I., Arata, Y. Dynamical structure of the antibody combining site as studied by <sup>1</sup>H-<sup>15</sup>N shift correlation NMR spectroscopy. *Biochemistry* 31:2464–2468, 1992.
40. Constantine, K.L., Goldfarb, V., Wittekind, M., Anthony, J., Ng, S.-C., Mueller, L. Sequential <sup>1</sup>H and <sup>15</sup>N NMR assignments and secondary structure of a recombinant antidigoxin antibody V<sub>L</sub> domain. *Biochemistry* 31:5033–5043, 1992.
41. Anthony, J., Near, R., Wong, S.-L., Iida, E., Ernst, E., Wittekind, M., Haber, E., Ng, S.-C. Production of a stable antidigoxin Fv in *Escherichia coli*. *Mol. Immun.* 29: 1237–1247, 1992.
42. Glockshuber, R., Malia, M., Pfizinger, I., Pluckthun, A. A comparison of strategies to stabilize immunoglobulin Fv fragments. *Biochemistry* 29:1362–1367, 1990.
43. States, D.J., Haberkorn, R.A., Ruben, D.J. A two-dimensional nuclear Overhauser experiment with pure absorption phase in four quadrants. *J. Magn. Reson.* 48:286–292, 1982.
44. Marion, D., Ikura, M., Bax, A. Improved solvent suppression in one- and two-dimensional NMR spectra by convolution of time domain data. *J. Magn. Reson.* 84:425–430, 1989.
45. Borgias, B.A., Gochin, M., Kerwood, D.J., James, T.L. Relaxation matrix analysis of 2D NMR data. *Prog. NMR Spectrosc.* 22:83–100, 1990.
46. Kamath, U., Shriver, J.W. Characterization of thermotropic state changes in myosin subfragment-1 and heavy meromyosin by UV difference spectroscopy. *J. Biol. Chem.* 264: 5586–5592, 1989.
47. Johnson, M.L. The analysis of ligand-binding data with experimental uncertainties in the independent variables. *Anal. Biochem.* 148:471–478, 1985.
48. Abragam, A. "The Principles of Nuclear Magnetism." Oxford, England: Clarendon Press, 1961.
49. Press, W.H., Flannery, B.P., Teukolsky, S.A., Vetterling, W.T. "Numerical Recipes: The Art of Scientific Computing." Cambridge, U.K.: Cambridge University Press, 1989.
50. Sheriff, S., Hendrickson, W.A., Smith, J.L. Structure of myohemerythrin in the azidomet state at 1.7/1.3 Å resolution. *J. Mol. Biol.* 197:273–296, 1987.
51. Case, D.A., Karplus, M. Dynamics of ligand binding to heme proteins. *J. Mol. Biol.* 132:342–368, 1979.
52. Connolly, M.L. Analytical molecular surface calculations. *J. Appl. Crystallogr.* 16:548–558, 1983.
53. Brunger, A.T. "X-PLOR (Version 2.1) Manual." New Haven, CT: Yale University Press, 1990.
54. Chothia, C., Novotny, J., Brucoleri, R., Karplus, M. Domain association in immunoglobulin molecules: The packing of the variable domains. *J. Mol. Biol.* 186:651–663, 1985.
55. Lipari, G., Szabo, A. Effect of librational motion on fluorescence depolarization and nuclear magnetic resonance relaxation in macromolecules and membranes. *Biophys. J.* 30:489–506, 1980.
56. Lipari, G., Szabo, A. Pade approximants to correlation functions for restricted rotational diffusion. *J. Chem. Phys.* 75:2971–2976, 1981.
57. Frauenfelder, H., Parak, F., Young, R.D. Conformational substates in proteins. *Annu. Rev. Biophys. Chem.* 17:451–479, 1988.
58. Kopple, K.D., Wang, Y.-S., Cheng, A.G., Bhandary, K.K. Conformations of cyclic octapeptides. 5. Crystal structure of cyclo (Cys-Gly-Pro-Phe)<sub>2</sub> and rotating frame relaxation (T<sub>1ρ</sub>) NMR studies of internal mobility in cyclic octapeptides. *J. Am. Chem. Soc.* 110:4168–4176, 1988.
59. Bruschweiler, R., Blackledge, M., Ernst, R.R. Multi-conformational peptide dynamics derived from NMR data: A new search algorithm and its application to antamanide. *J. Biomol. NMR* 1:3–11, 1991.
60. Woodward, C.K., Simon, I., Tuchsén, E. Hydrogen exchange and the dynamic structure of proteins. *Mol. Cell. Biochem.* 48:135–160, 1982.
61. Englander, S.W., Kallenbach, N.R. Hydrogen exchange and structural dynamics of proteins and nucleic acids. *Quart. Rev. Biophys.* 16:521–655, 1984.
62. Lumry, R., Rosenberg, A. The mobile defect hypothesis of protein function. *Col. Int. C.N.R.S. L'Eau Syst. Biol.* 246: 55–63, 1975.
63. Englander, S.W. Measurement of structural and free energy changes in hemoglobin by hydrogen exchange methods. *Ann. N.Y. Acad. Sci.* 244:10–27, 1975.
64. Gregory, R.B., Lumry, R. Hydrogen-exchange evidence for distinct structural classes in globular proteins. *Biopolymers* 24:301–326, 1985.
65. Pedersen, T.G., Sigurskjold, B.W., Andersen, K.V., Kjaer, M., Poulsen, F.M., Dobson, C.M., Redfield, C. A nuclear magnetic resonance study of the hydrogen-exchange behavior of lysozyme in crystals and solution. *J. Mol. Biol.* 218:413–426, 1991.
66. Ringe, D., Petsko, G.A. Mapping protein dynamics by X-ray diffraction. *Prog. Biophys. Mol. Biol.* 45:197–235, 1985.
67. Willis, B.T.M., Pryor, A.W. "Thermal Vibrations in Crystallography." Cambridge, U.K.: Cambridge University Press, 1985.
68. Kidera, A., Inaka, K., Matsushima, M., Go, N. Normal mode refinement: Crystallographic refinement of protein dynamic structure applied to human lysozyme. *Biopolymers* 32:315–319, 1992.
69. Sheriff, S., Hendrickson, W.A., Stenkamp, R.E., Sieker, L.C., Jensen, L.H. Influence of solvent accessibility and intermolecular contacts on atomic mobilities in hemerythrin. *Proc. Natl. Acad. Sci. U.S.A.* 82:1104–1107, 1985.

**APPENDIX**  
**Primary Relaxation Data, Hydrogen Exchange Rates, Hydrogen Bonding, and Distances**  
**to the Solvent Accessible Surface**

Residue	$T_1$ (ms)	$T_2$ (ms)	NOE*	$k_{ex}$ (min <sup>-1</sup> )	$r_{surf}(\text{\AA})^\dagger$
Val-2	707 ± 22	100 ± 4	0.77	$> 3 \times 10^{-2}$	2.63
Val-3	703 ± 18	81 ± 3	0.72	$> 3 \times 10^{-2}$	1.46
Met-4	721 ± 11	85 ± 2	0.80	$> 3 \times 10^{-2}$	0.70
Thr-5 <sup>‡</sup>	739 ± 12	82 ± 2	0.82	$(1.1 \pm 0.1) \times 10^{-3}$	2.44
Gln-6	663 ± 20	61 ± 3	0.83	$> 3 \times 10^{-2}$	0.95
Thr-7	685 ± 12	74 ± 2	0.80	$(6.8 \pm 0.8) \times 10^{-3}$	2.58
Leu-9	692 ± 7	94 ± 1	0.82	$(9.8 \pm 0.5) \times 10^{-6}$	0.65
Ser-10	685 ± 6	99 ± 1	0.77	$> 3 \times 10^{-2}$	0.64
Leu-11 <sup>‡</sup>	687 ± 8	98 ± 2	0.79	$(1.5 \pm 0.1) \times 10^{-3}$	3.85
Val-13 <sup>‡</sup>	690 ± 8	87 ± 2	0.78	$(1.5 \pm 0.1) \times 10^{-4}$	3.65
Leu-15	722 ± 7	89 ± 1	0.80	$> 3 \times 10^{-2}$	0.65
Gly-16 <sup>‡</sup>	721 ± 11	91 ± 2	0.86	$(8.4 \pm 0.8) \times 10^{-3}$	1.86
Asp-17**	665 ± 6	83 ± 1	0.79	$(1.4 \pm 0.1) \times 10^{-4}$	2.64
Gln-18	743 ± 11	93 ± 2	0.81	$\sim 3 \times 10^{-2}$	0.65
Ala-19 <sup>§</sup>	694 ± 10	93 ± 2	0.74	$(5.3 \pm 0.1) \times 10^{-5}$	3.06
Ser-20	737 ± 9	96 ± 2	0.82	$> 3 \times 10^{-2}$	0.80
Ile-21 <sup>‡</sup>				$(2.9 \pm 0.1) \times 10^{-5}$	2.36
Ser-22	677 ± 10	85 ± 2	0.84	$(4.6 \pm 0.2) \times 10^{-4}$	2.13
Cys-23 <sup>‡</sup>	697 ± 12	75 ± 2	0.85	$(7.9 \pm 0.2) \times 10^{-5}$	1.21
Arg-24**	704 ± 12	69 ± 2	0.79	$(4.0 \pm 0.1) \times 10^{-4}$	2.75
Ser-25 <sup>‡</sup>	674 ± 14	81 ± 2	0.87	$(1.0 \pm 0.1) \times 10^{-3}$	2.52
Ser-26	686 ± 15	79 ± 2	0.82	$> 3 \times 10^{-2}$	1.75
Gln-27	687 ± 11	87 ± 2	0.78	$(7.9 \pm 0.4) \times 10^{-3}$	2.37
Leu-29 <sup>‡</sup>	689 ± 21	89 ± 4	0.80	$> 3 \times 10^{-2}$	3.61
Val-30	642 ± 11	90 ± 2	0.91		2.40
His-31 <sup>‡</sup>	704 ± 18	89 ± 3	0.95	$> 3 \times 10^{-2}$	3.28
Ser-32	674 ± 15	80 ± 2	0.78	$> 3 \times 10^{-2}$	0.74
Asn-33 <sup>§</sup>	654 ± 40	82 ± 1	0.82	$> 3 \times 10^{-2}$	2.50
Gly-34 <sup>§</sup>	673 ± 14	98 ± 3	0.82	$> 3 \times 10^{-2}$	0.95
Asn-35 <sup>§</sup>	724 ± 14	78 ± 2	0.84	$> 3 \times 10^{-2}$	1.98
Thr-36	750 ± 18	91 ± 3	0.85	$> 3 \times 10^{-2}$	0.65
Tyr-37**	770 ± 28	95 ± 4	0.81	$(3.1 \pm 0.1) \times 10^{-3}$	4.33
Leu-38	692 ± 28	95 ± 5	0.86	$(6.8 \pm 0.5) \times 10^{-5}$	3.25
Asn-39 <sup>‡</sup>	592 ± 32	92 ± 8	0.81	$(6.8 \pm 2.2) \times 10^{-5}$	4.82
Trp-40 <sup>§</sup>	677 ± 16	61 ± 2	0.84	$(2.7 \pm 0.1) \times 10^{-5}$	4.50
Tyr-41 <sup>§</sup>	701 ± 15	88 ± 3	0.86	$(1.4 \pm 0.1) \times 10^{-5}$	4.03
Gln-43 <sup>‡</sup>	773 ± 61	70 ± 3	0.89	$> 2 \times 10^{-4}$	3.03
Lys-44	685 ± 14	85 ± 3	0.69	$> 3 \times 10^{-2}$	0.69
Ala-45	730 ± 6	98 ± 1	0.71	$> 3 \times 10^{-2}$	0.67
Gly-46	687 ± 15	122 ± 4	0.72	$(5.8 \pm 0.2) \times 10^{-4}$	0.64
Gln-47 <sup>§</sup>	676 ± 10	86 ± 2	0.75	$> 3 \times 10^{-2}$	1.83
Ser-48	707 ± 13	66 ± 2	0.73	$> 3 \times 10^{-2}$	1.21
Lys-50 <sup>§</sup>	711 ± 23	72 ± 3	0.74	$\sim 1 \times 10^{-2}$	2.26
Leu-51	708 ± 19	94 ± 4	0.78	$> 3 \times 10^{-2}$	0.67
Leu-52 <sup>§</sup>	655 ± 18	90 ± 3	0.85	$(1.6 \pm 0.1) \times 10^{-5}$	4.12
Ile-53	677 ± 14	90 ± 3	0.83	$(1.1 \pm 0.1) \times 10^{-5}$	5.46
Tyr-54**	666 ± 11	85 ± 2	0.80	$(8.1 \pm 0.2) \times 10^{-5}$	3.90
Val-56 <sup>§</sup>	680 ± 12	85 ± 2	0.84	$(1.3 \pm 0.1) \times 10^{-4}$	3.58
Ser-57 <sup>‡</sup>	758 ± 15	92 ± 3	0.83	$> 3 \times 10^{-2}$	1.78
Asn-58**	703 ± 17	76 ± 3	0.83	$(1.7 \pm 0.1) \times 10^{-3}$	2.77
Phe-60 <sup>§</sup>	694 ± 19	94 ± 4	0.79	$(9.8 \pm 0.4) \times 10^{-4}$	3.38
Ser-61	802 ± 17	64 ± 2	0.75	$> 3 \times 10^{-2}$	1.12
Gly-62	770 ± 23	99 ± 4	0.82	$> 3 \times 10^{-2}$	0.66
Val-63 <sup>‡</sup>	740 ± 8	91 ± 1	0.81	$(8.8 \pm 0.6) \times 10^{-3}$	1.76
Arg-66**	664 ± 12	92 ± 2	0.80	$> 3 \times 10^{-2}$	2.50
Phe-67 <sup>§</sup>	656 ± 8	78 ± 1	0.83	$(3.7 \pm 0.1) \times 10^{-4}$	2.99
Ser-68				$(1.7 \pm 0.1) \times 10^{-4}$	2.01

(continued)

**APPENDIX**  
**Primary Relaxation Data, Hydrogen Exchange Rates, Hydrogen Bonding, and Distances**  
**to the Solvent Accessible Surface (*Continued*)**

Residue	$T_1$ (ms)	$T_2$ (ms)	NOE*	$k_{\text{ex}}$ (min <sup>-1</sup> )	$r_{\text{surr}}$ (Å) <sup>†</sup>
Gly-69	686 ± 16	94 ± 3	0.81	$\sim 2 \times 10^{-2}$	1.26
Ser-70**				$(4.2 \pm 0.2) \times 10^{-4}$	3.50
Gly-71	694 ± 13	100 ± 3	0.86	$> 3 \times 10^{-2}$	0.65
Gly-73	634 ± 11	122 ± 3	0.78	$> 3 \times 10^{-2}$	1.22
Thr-74 <sup>§</sup>	708 ± 17	87 ± 3	0.79	$> 3 \times 10^{-2}$	1.39
Asp-75**	675 ± 10	85 ± 2	0.79	$\sim 2 \times 10^{-2}$	1.57
Phe-76 <sup>§</sup>				$(1.0 \pm 0.1) \times 10^{-4}$	0.90
Thr-77 <sup>‡</sup>	698 ± 17	88 ± 3	0.85	$(7.2 \pm 0.2) \times 10^{-5}$	2.23
Leu-78 <sup>‡</sup>	653 ± 12	93 ± 2	0.80	$(3.0 \pm 0.1) \times 10^{-5}$	3.71
Lys-79	673 ± 11	95 ± 2	0.79	$(4.3 \pm 0.1) \times 10^{-5}$	3.07
Ile-80 <sup>‡</sup>				$(2.9 \pm 0.1) \times 10^{-5}$	2.83
Ser-81 <sup>§</sup>	696 ± 9	87 ± 2	0.87	$(1.0 \pm 0.1) \times 10^{-3}$	1.57
Arg-82	714 ± 9	91 ± 2	0.75	$(1.9 \pm 0.1) \times 10^{-3}$	2.41
Val-83 <sup>‡</sup>				$(4.3 \pm 0.1) \times 10^{-5}$	3.65
Glu-84 <sup>‡</sup>	726 ± 12	88 ± 2	0.80	$(1.1 \pm 0.1) \times 10^{-4}$	2.99
Ala-85	723 ± 6	90 ± 1	0.79	$> 3 \times 10^{-2}$	0.65
Glu-86	693 ± 5	89 ± 1	0.80	$> 3 \times 10^{-2}$	0.79
Asp-87**	714 ± 8	77 ± 1	0.81	$(5.4 \pm 0.1) \times 10^{-5}$	3.56
Leu-88 <sup>§</sup>	674 ± 5	83 ± 1	0.79	$(9.8 \pm 0.2) \times 10^{-4}$	2.47
Gly-89	711 ± 8	99 ± 1	0.80	$(1.5 \pm 0.1) \times 10^{-4}$	1.59
Ile-90 <sup>‡</sup>	695 ± 12	84 ± 2	0.86	$(7.6 \pm 0.2) \times 10^{-5}$	2.00
Tyr-91 <sup>‡</sup>	699 ± 18	86 ± 3	0.88	$(3.7 \pm 0.6) \times 10^{-6}$	3.59
Phe-92 <sup>§</sup>	681 ± 15	77 ± 3	0.88	$(1.6 \pm 0.1) \times 10^{-5}$	3.88
Cys-93 <sup>‡</sup>	656 ± 13	93 ± 2	0.84	$(7.0 \pm 0.2) \times 10^{-5}$	4.82
Ser-94 <sup>‡</sup>	668 ± 15	87 ± 3	0.87	$(7.2 \pm 0.3) \times 10^{-5}$	5.13
Thr-96 <sup>§</sup>	893 ± 106	61 ± 2	0.95	$> 3 \times 10^{-2}$	3.62
Thr-97**	784 ± 22	86 ± 3	0.85	$\sim 2 \times 10^{-2}$	3.91
His-98 <sup>‡</sup>	711 ± 18	83 ± 3	0.86	$\sim 2 \times 10^{-2}$	2.90
Gly-104 <sup>‡</sup>	678 ± 31	59 ± 6	0.83	$(4.9 \pm 1.0) \times 10^{-3}$	2.69
Gly-105	726 ± 21	66 ± 4	0.82	$> 3 \times 10^{-2}$	0.72
Gly-106**	712 ± 11	95 ± 2	0.80	$(3.3 \pm 0.1) \times 10^{-3}$	2.96
Thr-107**	710 ± 15	88 ± 3	0.81	$(7.0 \pm 0.3) \times 10^{-5}$	2.09
Lys-108 <sup>‡</sup>	668 ± 11	104 ± 3	0.78	$(3.3 \pm 0.2) \times 10^{-3}$	1.45
Leu-109**	695 ± 14	86 ± 2	0.84	$(5.5 \pm 0.1) \times 10^{-5}$	1.49
Glu-110**	691 ± 11	90 ± 2	0.73	$(3.3 \pm 0.1) \times 10^{-4}$	3.48
Ile-111	725 ± 6	92 ± 1	0.75	$\sim 1.0 \times 10^{-2}$	0.65
Lys-112 <sup>†</sup>	642 ± 7	115 ± 2	0.67	$> 3 \times 10^{-2}$	2.09
Arg-113	752 ± 4	170 ± 1	0.19	$> 3 \times 10^{-2}$	0.89

\*The NOE values are accurate to approximately  $\pm 0.1$  NOE units.

<sup>†</sup>Denotes minimum distance from the backbone HN atom to the solvent accessible surface (see Materials and Methods).

<sup>‡</sup>Indicates amide hydrogen-oxygen distance ( $r_{\text{HO}}$ ) < 2.00 Å.

<sup>§</sup>Indicates  $2.25 \text{ Å} \geq r_{\text{HO}} \geq 2.00 \text{ Å}$ .

\*\*Indicates  $2.50 \text{ Å} > r_{\text{HO}} > 2.25 \text{ Å}$ .